

# Estimating Monthly Global Ground-Level NO<sub>2</sub> Concentrations Using Geographically Weighted Panel Regression

## Abstract

Predicting long-term ground-level nitrogen dioxide (NO<sub>2</sub>) is important globally to support environmental and public health research and to provide information to governments and society for air pollution control policies. The ozone monitoring instrument (OMI), onboard Aura Satellite, detects monthly global tropospheric column amounts (TrCA) of NO<sub>2</sub> molecules. However, the relationship between the ground-level NO<sub>2</sub> concentration and TrCA of NO<sub>2</sub> molecules remains elusive because NO<sub>2</sub> molecules in the air are not vertically evenly distributed. We use the geographically weighted panel regression (GWPR) to examine the relationship among satellite-derived data, measured ground-level NO<sub>2</sub> concentration, and several controlling meteorological variables from January 2015 to October 2021. The GWPR can analyze unbalanced panel data and capture the spatial variability of the relationship. Based on the GWPR estimation, the 82 monthly global ground-level NO<sub>2</sub> concentrations are predicted from January 2015 to October 2021. The GWPR is reliable, indicated by the 10-fold cross-validation. The accuracy of raster prediction of global ground-level NO<sub>2</sub> from January 2015 to October 2021 is 69.61%. The coefficient of correlation, root mean square error and mean absolute error between globally predicted and measured ground-level NO<sub>2</sub> are 0.838, 7.84  $\mu\text{g}/\text{m}^3$  and 4.07  $\mu\text{g}/\text{m}^3$  during

the research period, while the mean of globally measured ground-level NO<sub>2</sub> is 19.47  $\mu\text{g}/\text{m}^3$ . Overall, this research provides critical basic data to environmental and public health science and valuable information for governments and societies to make more reasonable policies.

## Keywords

Monthly Ground-Level NO<sub>2</sub> Concentration; GWPR model; spatial non-stationarity; OMI

## Introduction

Air pollutant, nitrogen dioxide (NO<sub>2</sub>), is adversely related to various health outcomes (Lelieveld et al. 2015; Newell et al. 2017; Ogen 2020; Orellano et al. 2020). The relationship between all-cause mortality and NO<sub>2</sub> concentration is positive (Brunekreef and Holgate 2002). Specifically, a 10  $\mu\text{g}/\text{m}^3$  increase in NO<sub>2</sub> concentration in short-term is associated with a 0.72% increase in the relative risks of all-cause mortality (Orellano et al. 2020). The European Union and World Health Organization (WHO) recommend that the annual average exposure to ambient NO<sub>2</sub> should be lower than 40  $\mu\text{g}/\text{m}^3$ . Additionally, other air pollutants, such as particulate matter and ozone, are related to approximately 3.3 million premature deaths per year globally, and NO<sub>2</sub> is one of the critical ozone precursors (Beckerman et al. 2008; Lelieveld et al. 2015). Evidence shows a link between NO<sub>2</sub> and various acute and chronic diseases, especially decreased lung function and lung cancer

(Chiusolo et al. 2011; Hamra et al. 2015; Rice et al. 2013). Furthermore, several studies indicate that in areas with high NO<sub>2</sub> concentration, people are more easily infected by the coronavirus and more difficult to recover, controlling for several other crucial factors, including age, gender, restriction policy, among others (Li and Managi 2022; Ogen 2020; Wu et al. 2020; Yao et al. 2021). Besides, air pollution affects human well-being directly (Li and Managi 2021b). For example, an increase of 10  $\mu\text{g}/\text{m}^3$  in annual average NO<sub>2</sub> is related to a roughly 50% decrease of life satisfaction in London (Mackerron and Mourato 2009). The ground-level NO<sub>2</sub> concentration affects human well-being and public health the most (Lelieveld et al. 2015; Li and Managi 2021b, 2022). However, the satellite measurements focus mainly on the tropospheric column amounts (TrCA) and the total column amounts (ToCA) of NO<sub>2</sub> (**Figure 1**) (OMI Team 2012). The association ground-level NO<sub>2</sub> concentration with TrCA or ToCA remains unclear because the NO<sub>2</sub> molecules are not vertically evenly distributed in the air. Several recent studies investigate the regional ground-level NO<sub>2</sub> concentration based on satellite observations. For example, Kim et al. estimate the hourly near-surface NO<sub>2</sub> in Alpine domain from June 2018 to May 2020 (Kim et al. 2021); Li et al. detect the ground-level NO<sub>2</sub> concentrations in Wuhan urban agglomeration during 2019 (Li and Wu 2021; Li et al. 2020); and Qin et al. probe the ground-level NO<sub>2</sub> over Central-Eastern China from May 2013 to April 2014 (Qin et al. 2017). However, there is a lack of ground-level NO<sub>2</sub> concentration measurements in low-income countries, which induces broad uncertainty of ground-level NO<sub>2</sub> distribution (Larkin et al. 2017). In order to help to detect the adverse impacts of NO<sub>2</sub> on public health and human well-being, the global time-series ground-level NO<sub>2</sub> data is strongly desired.

Figure 1 is located here.

Geographically weighted regression (GWR) is an advanced method that estimates air pollution taking the spatial contexts into account (Bigdeli et al. 2021; Jiang et al. 2017). To examine the relationship between satellite-derived data and measured ground-level air pollution, a variety of models are developed, such as land-use regression (Bechle et al. 2015; Larkin et al. 2017), chemical transport model (Geddes et al. 2016), linear regression model (Lin et al. 2019; Liu et al. 2017), GIS-based multi-source and multi-box model (Wang and Chen 2013), geographically and temporally weighted regression (GTWR) (Li et al. 2020; Qin et al. 2017), and machine learning method (Kim et al. 2021). All these models show relatively high accuracy in the estimations. In order to further improve the accuracy, we take spatial variability of the relationship between satellite-derived data and measured ground-level air pollution into account. The GWR can illustrate the spatial variability of the relationship according to the local regression technique and spatial weights (Fotheringham and Oshan 2016; Hu et al. 2013). It must be noted that here the global models are not spatially global models but statistically global models. The statistically global models mainly investigate the conditional interactions between the dependent and independent variables on the complete data set, while the statistically local models are based on partial data set taking each observing subject as the center (Beenstock and Felsenstein 2019).

Currently, the GWR can only analyze the cross-sectional data (data collected by observing many subjects at one period of time) or the panel data (data collected by observing many subjects across time) by using pooled ordinary least squares (POLS). To incorporate the temporal effect into the analysis, there are two other advanced methods,

88 GTWR (Fotheringham et al. 2015; Qin et al. 2017) and geographically weighted panel  
89 regression (GWPR) (Yu et al. 2021), to regress the balanced panel data (data collected by  
90 observing many subjects at all periods during the study period). GTWR is a spatially and  
91 temporally non-stationary model. Integrating spatial and temporal distance into  
92 spatiotemporal distance poses fresh unknowns, though Euclidean distance is still a  
93 powerful tool (Fotheringham et al. 2015; Li and Managi 2021a; Qin et al. 2017).  
94 Furthermore, the recent GTWR model requires that the input data set should be a balanced  
95 panel data set (Gollini et al. 2015). Yu et al.'s GWPR improves GWR by using the least  
96 squares dummy variable estimator, but models with other effects, such as fixed effects and  
97 random effects, are under development (Yu et al. 2021). This method works when the panel  
98 data have only a handful of periods. Moreover, neither of these two methods can solve the  
99 problem with unbalanced panel data (except balanced panel data, all panel data are  
100 unbalanced) due to the issues in the spatially weighted matrix. However, this limitation in  
101 the GWPR model is induced by the current toolboxes in most statistical software rather  
102 than the GWPR algorithm, although none of the current toolboxes specifically addresses  
103 the GWPR. For example, the outstanding GWR package "GWmodel" in R can also execute  
104 GWPR in specific situations using pre-transformed data sets. Yet, this algorithm builds  
105 spatially weighted matrix rows for each observation, which consumes a large volume of  
106 computer memory and might cause failure due to a lack of memory. Furthermore, when it  
107 calibrates the adaptive distance bandwidth in GWPR using unbalanced panel data, it might  
108 mistake the numbers of spatial neighbors of some observations because the observation  
109 numbers vary in each location in unbalanced panel data. In fact, most observed data sets  
110 are unbalanced, including our data set. To analyze the panel data by GWPR and facilitate

other researchers, we bundle the GWPR algorithm into a new R package, “GWPR.light” (<https://cran.r-project.org/web/packages/GWPR.light/index.html>), and release it on CRAN (The Comprehensive R Archive Network). The “GWPR.light” requires less memory even in big data calculation, solves the issues in the numbers of spatial neighbors of observations, and can perform GWPR with fixed or random effects.

In this paper, firstly, according to a series of statistical tests and model comparisons, we choose the GWPR with fixed time-fixed effects. This GWPR model excels at accuracy. Secondly, the GWPR analysis involves several auxiliary variables, including terrain atmospheric pressure, land surface temperature, normalized difference vegetation index (NDVI), precipitation, planetary boundary layer height (PBLH), and year dummy variables, to detect the relationship between ground-level and TrCA of NO<sub>2</sub>. Thirdly, we calibrate the optimal bandwidth, critical to building the spatially weighted matrix. Fourthly, we estimate the spatially non-stationary coefficients using the GWPR model, then interpolate the coefficients into raster data. Finally, we provide the monthly global ground-level NO<sub>2</sub> concentration from January 2015 to October 2021.

## **Materials and Methodology**

### ***Materials***

#### *Satellite-Derived NO<sub>2</sub> Estimation*

The satellite instrument, Ozone Monitoring Instrument (OMI), provides vertical column amounts of NO<sub>2</sub>. The OMI/Aura NO<sub>2</sub> Total and Tropospheric Column Daily L2 Global Gridded 0.25 degree × 0.25 degree V3 (OMNO2G) is the global daily grids data set

with a 0.25-degree resolution to gauge TrCA and ToCA of NO<sub>2</sub> (**Figure 1**) based on the observation of the NASA Earth Observing System (EOS) Aura satellite platform (Irie et al. 2012; Li and Wu 2021; Nickolay et al. 2019) ([https://disc.gsfc.nasa.gov/datasets/OMNO2G\\_003/summary](https://disc.gsfc.nasa.gov/datasets/OMNO2G_003/summary)). This satellite was launched on July 15<sup>th</sup> 2004, and began providing daily global TrCA, stratospheric column amounts and ToCA of NO<sub>2</sub> observation (unit: *molecules/cm<sup>2</sup>*) from October 1<sup>st</sup> 2004 (Nickolay et al. 2019; OMI Team 2012). The OMI-NO<sub>2</sub> data sets, especially the OMNO2G, have been widely used in emission and pollution monitoring (Curier et al. 2014; Li and Wu 2021; Liu et al. 2017). Air pollution near the surface impacts human health and daily life the most harmfully (Hamra et al. 2015; Rice et al. 2013). However, the ground-level NO<sub>2</sub> concentration is unavailable in many areas, particularly in rural areas and most developing countries. Therefore, the conversion or the estimation from TrCA or ToCA to ground-level data becomes a critical point. The EOS Aura orbit is a sun-synchronous polar orbit at an altitude of 705 km, and the satellite goes over each location between the local time 12:00 and 15:00 (OMI Team 2012; Schoeberl et al. 2006). Due to the orbit altitude, the ToCA of NO<sub>2</sub> covers the NO<sub>2</sub> molecules in the troposphere, stratosphere, mesosphere, and thermosphere, while TrCA of NO<sub>2</sub> takes those in only the troposphere into account. Because the troposphere is most affected by human activities and air pollution, there has the most substantial impact on human health (Lelieveld et al. 2015; Li and Managi 2022) and well-being (Li and Managi 2021b), the TrCA of NO<sub>2</sub> is an ideal independent variable to predict the ground-level NO<sub>2</sub> concentration. However, owing to anthropogenic climate change, tropopause height is slowly rising (Meng et al. 2021). Though this continuous rise is relatively tiny in comparison to the tropopause height, whether it influences the

estimation of the TrCA of NO<sub>2</sub> remains elusive. In order to choose the satellite NO<sub>2</sub> variable, we put both the ToCA and TrCA of NO<sub>2</sub> in the analyses as the primary variable, respectively. Both the goodness of fit of the model taking the TrCA of NO<sub>2</sub> as the dependent variable (R<sup>2</sup>: 74.45%) and cross validation results are slightly better than the other model using the ToCA of NO<sub>2</sub> (R<sup>2</sup>: 74.39%). Moreover, compared with satellite orbit height, the tropopause height is closer to the surface, which might make TrCA of NO<sub>2</sub> more accurate. Therefore, the TrCA of NO<sub>2</sub> is employed in the final analysis.

We convert the unit of the TrCA of NO<sub>2</sub> from *molecules/cm<sup>2</sup>* to microgram per square meter (*μg/m<sup>2</sup>*), to make it understandable to the public, as follows:

$$ATrCA = RTrCA/N_A \times MM_{NO_2} \times 10,000 \text{ cm}^2/\text{m}^2 \times 1,000,000 \text{ } \mu\text{g/g} \quad (1)$$

where *ATrCA* is the TrCA of NO<sub>2</sub> after the unit conversion, whose unit is *μg/m<sup>2</sup>*, *RTrCA* is the value extracted from the OMNO2G directly, whose unit is *molecules/cm<sup>2</sup>*, *N<sub>A</sub>* is the Avogadro constant ( $6.022 \cdot 10^{23} \text{ mol}^{-1}$ ), and *MM<sub>NO2</sub>* is the molar mass of NO<sub>2</sub> (46.007 *g/mol*).

The temporal resolution of our analysis is monthly, although both the OMNO2G and ground-level measurements are seemingly daily. Due to the orbit height of the EOS Aura, the satellite revisit period is 16 days and the orbit period is 98.83 minutes (Schoeberl et al. 2006). The EOS Aura's telescope field of view is 2600km on the ground. Its daily data are from day lit portion of the satellite's 14 orbits. For all these reasons, each location could be observed several times in a month rather than every day, i.e., some locations are unobserved in a few days. Furthermore, other auxiliary satellite data, such as land surface temperature, NDVI, among others, are obtained from EOS Terra and Aqua satellites,



whose satellite revisit periods are also 16 days. For these reasons, we convert the daily TrCA of NO<sub>2</sub> from the OMNO2G data set into the monthly average TrCA of NO<sub>2</sub>.

### *Ground-Level NO<sub>2</sub> Measurements*

This data set can be downloaded from the Air Quality Open Data Platform (<https://aqicn.org/data-platform/covid19/>). The data have been available in over 530 major cities since 2015. The data provider has converted to the unified unit, part per billion (PPB), in accordance with the requirement of the United States Environmental Protection Agency. Initially, the data set included 539 cities, but nine were dropped, owing to its no more than five monthly records from January 2015 to October 2021. This study exploits the monthly average NO<sub>2</sub> concentration as the dependent variable, calculated from the daily data, to merge with the satellite data correctly. The Air Quality Open Data Platform also provides the locations of the cities with measurement points (<https://aqicn.org/data-platform/covid19/airquality-covid19-cities.json>) (**Figure 2, Supplementary Materials Table S1: City List**). In most cities, there are generally several measurement points. The data set records the medians of ground-level NO<sub>2</sub> in view of the data from different measurement points in a specific city. The ground-level measured NO<sub>2</sub> concentration data are daily. To connect them with the satellite data, we convert them into monthly average values. It must be underscored that we use all the daily observations to calculate the monthly mean of ground-level NO<sub>2</sub>, but there is no significant difference between the means using all the daily observations and using the observations sampled at OMI measurement dates. The correlation between the means in each measurement using all the daily observations and using the observations sampled at OMI measurement dates is 0.980

( $p$ -value < 0.1%). The variation caused by the difference is only 4.17% of the total variation of the means using all daily observations. Therefore, the means of all the daily observations are valid. Additionally, the OMNO2 is a Level-2 grid product. The missing values of the satellite measurement appear in the data swath gaps. Even though the satellite does not observe a specific city on a certain day, other grids close to that city might be detected. Thus, ignoring some ground-level measurements due to no satellite data might decrease the accuracy of predictions.

*Figure 2 is located here.*

The unit of monthly average ground-level measured NO<sub>2</sub> concentration data is PPB, while the unit of the monthly average TrCA of NO<sub>2</sub> is microgram per square meter ( $\mu\text{g}/\text{m}^2$ ). To make the units of these two data sets consistent, we convert the unit of monthly average ground-level measured NO<sub>2</sub> concentration data from PPB to  $\mu\text{g}/\text{m}^3$  by the following equation:

$$GNO2 = \frac{P \times MW_{NO2} \times RGN02}{R \times T \times 1000} \quad (2)$$

where  $GNO2$  is the monthly average ground-level NO<sub>2</sub> concentration with unit  $\mu\text{g}/\text{m}^3$ ,  $RGN02$  is the NO<sub>2</sub> concentration before conversion, whose unit is PPB,  $P$  is the terrain atmospheric pressure (mmHg), which could be extracted from OMNO2G and converted into the monthly average values (OMNO2G data unit is hPa, and the conversion coefficient between mmHg and hPa is 0.750 mmHg/hPa),  $MW_{NO2}$  is 46.007,  $R$  is the ideal gas constant ( $62.4 \text{ L} \cdot \text{Torr} \cdot \text{K}^{-1} \cdot \text{mol}^{-1}$ ), and  $T$  is the monthly average temperature from MODIS product, MOD11C3.

## 221 *Auxiliary Data*

222 Auxiliary data, including terrain atmospheric pressure, temperature, NDVI,  
223 precipitation, and PBLH, are taken as the control variables to improve the model's  
224 performance. A considerable amount of previous studies involve terrain atmospheric  
225 pressure in the analyses of NO<sub>2</sub> concentration (Chi et al. 2021; Li et al. 2020). Terrain  
226 atmospheric pressure data are from OMNO2G, with a 0.25-arc-degree resolution.  
227 Although the temporal resolution of this data set is daily, it has the same problem as the  
228 TrCA of NO<sub>2</sub> data set, a long satellite revisit period of Aura satellite. So, we convert it into  
229 a monthly average value. Additionally, to make the calculation understandable, the unit of  
230 land surface temperature has been converted into Celsius.

231 The temperature data are provided by the Moderate Resolution Imaging  
232 Spectroradiometer (MODIS, <https://modis.gsfc.nasa.gov/>). The products, MOD11C3 and  
233 MYD11C3, are based on the MODIS Terra and Aqua satellites' observations and  
234 measurements, including the day-time and nighttime average temperature, with a 0.05-arc-  
235 degree spatial resolution (<https://modis.gsfc.nasa.gov/data/dataproduct/mod11.php>). Due to  
236 the 16-day revisit period, there are one or two global raster data based on each satellite's  
237 observation every month. In a month, we take the mean of all the raster data, involving the  
238 day-time and nighttime average temperature in a month, to obtain the monthly average  
239 temperature raster. Of note, the spatial resolution of the monthly average temperature raster  
240 is still 0.05 arc degree. To make it consistent with the monthly average TrCA of NO<sub>2</sub>, we  
241 reduce the resolution to 0.25 arc degree, by applying the average value.

242 The monthly NDVI data are acquired from the MODIS products, MOD13C2 and  
243 MYD13C2 (<https://modis.gsfc.nasa.gov/data/dataproduct/mod13.php>), with a 0.05-arc-

degree spatial resolution. We also use the average value to make its resolution become 0.25 arc degree. The NVDI value ranges from -1 to 1. Because the ground-level NO<sub>2</sub> data is from cities, the situation in rural areas is not carefully gauged. To enable the model to predict the environment in rural areas, we incorporated the NDVI into the analysis since the most notable difference between urban and rural areas is landscape and human activity density. Both the NDVI and land cover raster could depict landscape, but land cover data is discrete and yearly, not applicable for this analysis. Therefore, we employ the NDVI to slash the influence of the difference between urban and rural areas. Additionally, nighttime light is associated with transportation (Chang et al. 2019) and human activity (Zhao et al. 2019), which are related to air pollution emissions. To represent their impacts, we also put the nighttime light data into the initial model. However, this has little effect on the prediction accuracy. Hence, it is removed in the final model.

The precipitation data are obtained from NASA Global Land Data Assimilation System Version 2 (GLDAS) Noah Land Surface Model L4 monthly 0.25 x 0.25 degree V2.1 (GLDAS\_NOAH025\_M, [https://disc.gsfc.nasa.gov/datasets/GLDAS\\_NOAH025\\_M\\_2.1/summary](https://disc.gsfc.nasa.gov/datasets/GLDAS_NOAH025_M_2.1/summary)). The temporal and spatial resolutions are one month and 0.25 arc degree, respectively. This data set has some missing values because some regions are too close to the seas and oceans. To avoid the reduction of the data size in our calculation, we impute the missing values by averaging their closest surrounding grids. We estimate the data set twice, that is, the original GLDAS\_NOAH025\_M data set boundary extends roughly 0.5 arc degree into the seas and oceans. The original unit of this data set is  $kg/(m^2 \cdot s)$ , but the most values are less than

0.0001  $kg/(m^2 \cdot s)$ . To improve the readability and robustness of the calculation, we convert its unit to  $kg/(m^2 \cdot h)$ .

The PBLH data are extracted from Monthly mean, Time-Averaged, Single-Level, Assimilation, Surface Flux Diagnostics V5.12.4 (M2TMNXFLX, [https://disc.gsfc.nasa.gov/datasets/M2TMNXFLX\\_5.12.4/summary](https://disc.gsfc.nasa.gov/datasets/M2TMNXFLX_5.12.4/summary)). The spatial resolution of this data set is  $0.5^\circ \times 0.625^\circ$ . We employ the bilinear interpolation method to impute a new data set with a 0.25-arc-degree resolution. The unit of PBLH is meter (m).

**Figure 3** demonstrates the variable selection process of this research. Simply speaking, we select a variable that meets one of the following three requirements. Firstly, the variable is significantly related to the dependent variable and has low correlations with other variables in the model. Secondly, the variable can improve the model accuracy significantly. Thirdly, previous studies prove that the variable is necessary for the analysis. In the model design stage, we consider many other variables, including humidity, nighttime light, wind speed, cloud pressure, aerosol optical depth, ultraviolet aerosol index, among others. However, none of these variables are effective due to either their poor improvement in the prediction accuracy or the multicollinearity between independent variables. For example, the correlation coefficient between humidity and precipitation significantly exceeds 0.5. Furthermore, the correlation coefficient between humidity and temperature is over 0.7, while the relationship between precipitation and temperature is not so strong, only 0.15. Therefore, we keep the precipitation and temperature in the analysis. Moreover, the results of GWPR are spatial point data frames. To secure the coefficient raster data for the prediction, we have to employ interpolation methods, which would apparently cause some slight errors. If the benefit from involving one more variable cannot offset the errors in its

interpolation, it should not be taken into account. In view of numerous tests, finally, we select the TrCA of NO<sub>2</sub>, terrain atmospheric pressure, temperature, NDVI, precipitation, and PBLH as independent variables.

*Figure 3 is located here.*

### *Descriptive Statistics*

We establish an unbalanced dataset based on the above data sources for modeling and prediction with time stamps and geographical locations from January 2015 to October 2021. The number of complete observations in this data set is 29,686. The unbalance of data expresses in both temporal and spatial extent. Every city has at least five-month, and at most 65-month data, i.e., it is the imbalance in temporal extent. Moreover, the spatial distribution is also unbalanced. For instance, the smallest distance between the two closest cities is 0.103 arc degree, while the largest distance is 24.710 arc degrees. As shown in **Figure 2**, most cities with the data are located in Northern Hemisphere, while only a few of them distribute in South America, Africa, and Australia, which drives increased difficulty of the interpolation.

**Figure 4** summarizes the statistical distributions and descriptive statistics of the variables in the original data set. The statistical distribution of concentration of ground-level NO<sub>2</sub> is one peak and right-skewed because the skewness is 7.17. Due to the 4.17 skewness, the statistical distribution of the monthly TrCA of NO<sub>2</sub> is one right-skewed peak. The statistical distribution of terrain atmospheric pressure is one left-skewed peak, whose skewness is -2.37. The shape of the monthly average temperature distribution is one

slightly left-skewed peak because of its skewness of -0.39. The statistical distribution of NDVI is one peak and slightly left-skewed (skewness: -0.34). The shape of its statistical distribution of precipitation is one right-skewed peak because its skewness is 2.25. The statistical distribution of the PBLH is one right-skewed peak (skewness: 1.79). According to the variable distribution shape illustrated in **Figure 4**, some variable distributions cannot be deemed as the normal distribution. So, directly putting them into regression is unsuitable. Putting another way, the POLS cannot be employed as the basic analysis model.

We choose the fixed effect model (FEM) as the basic algorithm based on a series of statistical tests. This will be described in the next section. In FEM, the data are transformed as follows:

$$\tilde{V}_{it} = V_{it} - \bar{V}_t \quad (3)$$

where  $\tilde{V}_{it}$  denotes the transformed dependent and independent variables in measurement  $i$  during  $t$  month,  $V_{it}$  denotes the original dependent and independent variables in measurement  $i$  during  $t$  month, and  $\bar{V}_t$  denotes the mean values of each original variable in measurement  $i$ . **Figure 5** demonstrates the variable distributions in the transformed data set. The variables in the transformed data set are almost normally distributed because their skewnesses and kurtosises are close to 0 except ground-level NO<sub>2</sub>, monthly TrCA of NO<sub>2</sub>, and precipitation. The distributions of those three variables in the transformed data set are right-skewed and leptokurtic because their skewnesses are 11.74, 4.00, and 1.68, and their kurtosises are 556.92, 54.23, and 10.11, respectively. We find that the transformed data set still has 17 extremely large numbers in ground-level NO<sub>2</sub>, which are more than ten standard deviations far from the mean. They mainly appear in five cities, including Izmir (Turkey), Konya (Turkey), Khorramabad (Iran), Qom (Iran), and Puebla (Mexico). If we ignore these

extreme numbers, the skewness and kurtosis decrease significantly. It must be underscored that the extreme numbers in the transformed data set mean that the variable in specific measurements fluctuated significantly, rather than that they are absolutely large. The variables, monthly TrCA of NO<sub>2</sub> and precipitation, show similar situations, though the extreme values appear in different cities. Because the share of the extreme numbers is no more than 0.5%, their impacts on regression can be ignored.

*Figures 4 and 5 are located here.*

**Figures 6 and 7** show the linear trends and correlation coefficients between the concentration of ground-level NO<sub>2</sub> and other variables in original and transformed data sets, respectively. In **Figures 6 and 7**,  $r$  and  $p$  represent Pearson's correlation coefficient and p-value, respectively (Taylor 1990). The  $r$  is calculated as follows:

$$r = \frac{\sum_{i=1}^n (X1_i - \bar{X1})(X2_i - \bar{X2})}{\sqrt{\sum_{i=1}^n (X1_i - \bar{X1})^2} \sqrt{\sum_{i=1}^n (X2_i - \bar{X2})^2}} \quad (4)$$

where  $r$  is the correlation coefficient,  $X1$  and  $X2$  are the aimed variables put into the test, and  $n$  is the data size. To estimate the significance of the correlation coefficient, we calculate the t-test value ( $t$ ), at first:

$$t = \frac{r\sqrt{n-2}}{\sqrt{1-r^2}} \quad (5)$$

Here, the p-value ( $p$ ) is calculated as follows:

$$p = 2 \times \Pr(T > t) \quad (6)$$

where  $T$  follows a t distribution with  $n - 2$  degrees of freedom, and  $\Pr(T > t)$  represents the probability of  $T > t$ . According to **Figures 6 and 7**, all correlation coefficients are significant at the 0.1% level.



Figures 6 and 7 are located here.

## **Methodology**

### *Spatially Stationary Global Model*

We first assume that the relationships between the ground-level concentration of NO<sub>2</sub> and other independent variables are spatially stationary. Those relationships do not vary by spatial contexts (Brunsdon et al. 1998; Fotheringham et al. 2002). We apply the three typical global models, the random effects model (REM), FEM, and POLS, to estimate the relationships among the variables. The only difference among these three global models is the time-fixed effects in the models. Therefore, substantial tests about the time-fixed effects are required.

We select global models with different time-fixed effects, namely, REM, FEM, and POLS. In order to compare FEM with POLS, we apply the F test for individual effects. FEM is better than POLS since the test result is significant, and the null hypothesis that no time-fixed effects are needed is rejected (Breusch and Pagan 1980; Croissant and Millo 2008). Based on the Breusch-Pagan Lagrange Multiplier test for random effects, the significant result indicates that REM is appropriate because the null hypothesis that no time-fixed effects are needed is not accepted, either (Breusch and Pagan 1980). We also run the Hausman test to detect the reasonable model between FEM and REM (Kang 1985). The significant result indicates FEM is preferred, as the null hypothesis that the preferred model is REM is rejected. Here, FEM in our analysis is illustrated as follows:

$$GNO2_{it} = \beta X'_{it} + \alpha_i + \mu_{it} \quad (7)$$

where  $GN02_{it}$  denotes the monthly average ground-level concentration of  $NO_2$  ( $\mu g/m^3$ ) in measurement  $i$  during  $t$  month,  $\mathbf{X}_{it}$  denotes a matrix of independent variables, including TrCA of  $NO_2$  ( $\mu g/m^2$ ), terrain atmospheric pressure (hPa), temperature ( $^{\circ}C$ ), NDVI, precipitation ( $kg/(m^2 \cdot h)$ ), PBLH (m), and year dummy variables in measurement  $i$  during  $t$  month,  $\alpha_i$  denotes the time-fixed effects,  $\mu_{it}$  denotes an idiosyncratic error, and  $\beta$  is a vector of parameters to be estimated. Some ignored variables, such as air pollution policy in countries, economic status, among others, are changed year by year. We, therefore, add the year dummy variables to the model.

### *Spatially Non-stationary Local Model*

Unlike global linear regression models, including REM, FEM, and POLS, the GWPR allows the coefficients to vary spatially (Brunsdon et al. 2010; Fotheringham and Oshan 2016). Because the relationship between the dependent variable and the independent variables could vary by the spatial context, the estimation accuracy of ground-level  $NO_2$  concentration, such as the goodness of fit of models, dramatically improves. Basically, the GWPR divides the total sample into numerous sub-samples, according to the optimal bandwidth and spatially weighted matrix. The bandwidth in GWPR is the threshold distance to judge whether two objects have a spatial relationship (Beenstock and Felsenstein 2019; Brunsdon et al. 2010; Brunsdon et al. 1998). If two objects have a spatial relationship, they are considered as the neighbors of each other. Currently, two types of bandwidth are widely used, fixed distance bandwidth and adaptive distance bandwidth (Gollini et al. 2015). Literally, the fixed distance bandwidth is a fixed threshold distance, and if two spatial objects are within this distance, they are spatially related. The adaptive

distance bandwidth is an integer of the number of objects in a subsample because every object always has a certain number of neighbors. Hence, the threshold distance for each object might be different. To calibrate the optimal bandwidth in the GWPR, the mean square prediction error is the critical index. When the mean square prediction error is the smallest, the model with a certain bandwidth has the highest accuracy (Gollini et al. 2015). Taking a specific bandwidth ( $b$ ), the mean square prediction error is calculated as follows:

$$MSPE(b) = \frac{m \sum_j [y_j - \widehat{y_j(b)}]^2}{(m - p + 1)^2} \quad (8)$$

where  $MSPE(b)$  is the mean square prediction error based on a specific bandwidth  $b$ ,  $m$  is the data size,  $y_j$  is the dependent variable's value of the  $j$ th record,  $\widehat{y_j(b)}$  is the predicted value of the  $j$ th record based on the bandwidth  $b$ , and  $p$  is the number of the parameters in the analysis. It must be noted that the bandwidth  $b$  can be either the fixed distance bandwidth or the adaptive distance bandwidth here. The GWPR is an improvement of GWR, considering time-fixed effects. In the GWR, previous studies generally assume that **Equation 8** is a U-shape function (Brunsdon et al. 1998; Fotheringham et al. 2002; Gollini et al. 2015). However, as those studies mentioned, there is no statistical or mathematical evidence for or against this assumption. The benefit from this assumption is the reduction of calculating time because the calculation could use the golden-section search to find the extremum to obtain optimal bandwidth (Gollini et al. 2015).

The step increment selection is applied to calibrate the optimal bandwidth due to the recently designed program that requires fewer computer resources. We calibrate the optimal fixed and adaptive distance bandwidths. In the fixed distance bandwidth selection, the selection extent is from 0.25 arc degree to 20 arc degrees, and the examined bandwidth

increases 0.25 arc degree every time because the spatial resolution of all the grid data is 0.25 arc degree. The optimal fixed distance bandwidth is 2.25 arc degrees (**Figure 8**). Since the spatial distribution of the cities with data is unbalanced and some points are far from others (**Figure 2**), many points would have no neighbor if using this bandwidth. Data islands severely destroy the stability of the GWPR because they have no relationship with other points in the data set. Both dropping the data islands and increasing the bandwidth would slash the accuracy of the analysis. Hence, we adopt the adaptive distance bandwidth. In the adaptive distance bandwidth selection, the selection extent is from 4 to 100, and the tested bandwidth increases one every time. When the adaptive distance bandwidth is less than 4, some local regressions do not have enough degrees of freedom. According to the analysis, the optimal adaptive distance bandwidth is selected, which is 7. In other words, in each subsample, every locally weighted regression involves seven cities' data.

*Figure 8 is located here.*

Spatially weighted matrix, based on the calibrated bandwidth, is calculated as follows:

$$\mathbf{w}_i = \begin{cases} [1 - (\frac{\mathbf{d}}{b_i})^2]^2, & d_k \in \mathbf{d} \text{ if } d_k \leq b_i \\ 0, & d_k \notin \mathbf{d} \text{ if } d_k > b_i \end{cases} \quad (9)$$

where  $\mathbf{w}_i$  denotes a vector of spatial weights between city  $i$  and its neighbors,  $\mathbf{d}$  represents a vector of distances between city  $i$  and its neighbors,  $b_i$  is the threshold distance of city  $i$ 's neighbors, and  $d_k$  is the distance between city  $i$  and city  $k$ . It should be emphasized that  $b_i$  might vary city by city, as here we use the adaptive distance bandwidth. Every vector is a column of the spatially weighted matrix. According to the spatial weights vectors, the total sample is divided into 530 sub-samples, taking every city as the center, respectively.

437 The GWPR estimates the coefficients in every location in light of the spatially  
 438 weighted matrix. In global model statistical tests, FEM is the preferred model, and in the  
 439 locally statistically test, most local regressions show significant time-fixed effects.  
 440 Therefore, the GWPR model is also following FEM. The GWPR model is expressed as  
 441 follows:

$$GNO2_{it} = \beta_i X'_{it} + \alpha_i + \epsilon_{it} \quad (10)$$

442 where  $\beta_i$  denotes a vector of parameters in the regression with the sub-sample taking the  
 443 city  $i$  as the center. In terms of the equation expression, the only difference between FEM  
 444 (**Equation 7**) and the GWPR based on FEM (**Equation 10**) is that  $\beta_i$  varies spatially. It  
 445 must be noted that the algorithm would change to the GWPR based on POLS if we directly  
 446 use the GWR method. According to cross validation, the accuracy and stability of the  
 447 GWPR based on POLS are lower than the GWPR based on FEM. In this way, the new  
 448 method, GWPR, is necessary for this analysis.

449 To estimate the coefficient in the GWPR, because the time-fixed effects ( $\alpha_i$ ) is  
 450 unknown (Croissant and Millo 2008), we need to expand **Equation 10**, as follows:

$$GNO2_{it} - \hat{\theta}_i \overline{GNO2}_i = (1 - \hat{\theta}_i) \beta_{0i} + \beta_i (X_{it} - \hat{\theta}_i \overline{X}_i)' + (\epsilon_{it} - \hat{\theta}_i \bar{\epsilon}_i) \quad (11)$$

451 where  $\hat{\theta}_i$  denotes the share of the individual effects in the total effects,  $\overline{GNO2}_i$  denotes the  
 452 mean of the ground-level NO2 concentration in the data set in the city  $i$ ,  $\beta_{0i}$  is the estimated  
 453 intercept in the city  $i$ ,  $\overline{X}_i$  denotes a vector of means of independent variables in the city  $i$ ,  
 454 and  $\bar{\epsilon}_i$  denotes the mean of the error in the city  $i$ . If the GWPR follows the data  
 455 transformation of FEM, the  $\hat{\theta}_i$  is always equal to 1. So  $\beta_{0i}$  is removed, in the GWPR based

456 on FEM. To simplify **Equation 11**, we define the matrix of independent variables  $\mathbf{x}_{it}$  and  
 457 the dependent variable  $gno2_{it}$  as follows:

$$\mathbf{x}_{it} = \mathbf{X}_{it} - \overline{\mathbf{X}_i} \quad (12)$$

$$gno2_{it} = GNO2_{it} - \overline{GNO2_i} \quad (13)$$

$$\sigma_{it} = \epsilon_{it} - \overline{\epsilon_i} \quad (14)$$

458 In the light of **Equations 12-14**, the GWPR model is transformed as follows:

$$gno2_{it} = \boldsymbol{\beta}_i \mathbf{x}'_{it} + \sigma_{it} \quad (15)$$

459 This algorithm becomes the typical GWR without the intercept. The coefficient estimation  
 460 could be displayed as follows:

$$\boldsymbol{\beta}_i = [\mathbf{x}_{it}^T \mathbf{W}_i \mathbf{x}_{it}]^{-1} \mathbf{x}_{it}^T \mathbf{W}_i gno2_{it} \quad (16)$$

461

## 462 *Statistical Indicators*

463 Previous studies widely use several statistical indicators, including  $R^2$ , root mean  
 464 square error (RMSE), mean absolute error (MAE),  $r$  between observed and predicted  
 465 values, and regression coefficients between observed and predicted values (Kim et al. 2021;  
 466 Li and Wu 2021; Liu et al. 2017), so we also apply to evaluate the estimation accuracy of  
 467 the GWPR model.  $R^2$  is a critical statistical indicator describing the goodness of fit. The  
 468 high  $R^2$  in the models means that the discrepancy between predicted  $NO_2$  concentration  
 469 and measured ground-level  $NO_2$  concentration is tiny. The  $R^2$  calculation algorithm is  
 470 shown as follows:

$$R^2 = 1 - \frac{\sum_{k=1}^n (MNO2_k - PNO2_k)^2}{\sum_{k=1}^n (MNO2_k - \overline{MNO2})^2} \quad (17)$$

where  $n$  represents the observation number in the total sample,  $MNO2_k$  represents the  $k$ th record of the measured ground-level  $NO_2$  concentration,  $PNO2_k$  represents the  $k$ th record of the predicted  $NO_2$  concentration, and  $\overline{MNO2}$  represents the mean of the measured ground-level  $NO_2$  concentration. It must be noted that this  $R^2$  of the GWR or the GPWR is the global value because here the total sample is used. The RMSE is also calculated, indicating the differences between predicted  $NO_2$  concentration and measured ground-level  $NO_2$  concentration. The RMSE is sensitive to both systematic error and random error, shown as follows:

$$RMSE = \sqrt{\frac{1}{n} \sum_{k=1}^n (MNO2_k - PNO2_k)^2} \quad (18)$$

The MAE is calculated as follows:

$$MAE = \text{mean}(|MNO2_k - PNO2_k|) \quad (19)$$

In the analysis, the MAE should be low. Additionally, the regression coefficients between observed and predicted values are imputed as follows:

$$MNO2_k = \alpha + \beta PNO2_k + \delta_k \quad (20)$$

where  $\alpha$  is the intercept in the regression and the ideal value of  $\alpha$  is 0,  $\beta$  is the slope and its ideal value is 1, and  $\delta_k$  is a random error term.

### *Spatial Interpolation of the Coefficients*

We use the ordinary Kriging (OK) method, described by the previous study (Li and Heap 2011), to interpolate the coefficients of the GWPR result into raster data. Directly using the GWPR result is insufficient to predict and obtain the ground-level  $NO_2$

concentration raster data because the result is a spatial point data frame and the coefficients spatially vary. The general form of the OK method is expressed (Pebesma 2004) as follows:

$$\hat{\beta}(s_0) = \sum_{l=1}^m \lambda_l \beta(s_l) \text{ with } \sum_{l=1}^m \lambda_l = 1 \quad (21)$$

where  $\hat{\beta}(s_0)$  represents the coefficient at unobserved location  $s_0$ ,  $\beta(s_l)$  represent the coefficient value at known location  $s_l$ ,  $\lambda_l$  is the spatial weight for the coefficient value at the  $l$ th location, and  $m$  is the number of known values. To obtain optimal  $\lambda_l$ , there are two requirements in OK: unbiased and minimal variance of estimation. If  $\sum_{l=1}^m \lambda_l$  is equal to 1, then it is unbiased (Pebesma 2004). To minimize the estimation variance, we use the spherical semi-variance mathematical model. Harnessing the OK method, the GWPR results would be estimated to several coefficient raster data with a 0.25-arc-degree spatial resolution. Additionally, the mean value raster data of variables are also interpolated by the OK method. In the prediction process, the data transformations following **Equations 12** and **13** are necessary. To check the reliability of the interpolation process, we apply the leave-one-out cross validation. Simply, the leave-one-out cross-validation requires the number of folds equals the numbers of cities in our data set. In the cross validation process, one certain city is selected as the test set, while all other 529 cities are used as the training set. This process will repeat 530 times until all the cities have been selected as the test set.

### *Predictions of Ground-level NO<sub>2</sub> Concentration and Change Trends*

The monthly global ground-level NO<sub>2</sub> concentration raster data are predicted based on the original raster data, coefficient rasters, and mean value rasters, following **Equation 15**. Furthermore, because the ground-level NO<sub>2</sub> concentration cannot be minus, any value less than zero is set to zero in the prediction grid data. The prediction process creates 82-



month grid data. To detect the monthly change trends of each grid, the monthly NO<sub>2</sub> concentrations of each grid are regressed with their month order. The first month of our data set is January 2015, so the month order of data in January 2015 is the 1<sup>st</sup>. Lastly, the month order of October 2021 is the 82<sup>nd</sup>. The monthly change trends are estimated as follows:

$$PNO2_{LT} = \alpha_L + \beta_L MO_T + \varphi_{LT} \quad (22)$$

where  $PNO2_{LT}$  is the predicted NO<sub>2</sub> concentration in the grid  $L$  in the  $T$ th month,  $MO_T$  is the month order of  $PNO2_{LT}$ ,  $\alpha_L$  is the intercept in the grid  $L$ ,  $\beta_L$  is the monthly NO<sub>2</sub> concentration change trend in the grid  $L$ , and  $\varphi_{LT}$  is a random error term. It must be noted that the data from a certain grid should be performed the regression once if there are no less than 30 records. Additionally, every individual regression just uses the data from one grid.

## Results

### *Validation of the GWPR Result*

The overall accuracy of the GWPR based on FEM is 74.45%, the RMSE is 7.171  $\mu g/m^3$ , and the is MAE 3.48  $\mu g/m^3$ . The mean of globally measured ground-level NO<sub>2</sub> is 19.47  $\mu g/m^3$ . **Figure 9** shows the relationship between predicted and measured ground-level NO<sub>2</sub> concentrations in the GWPR, and all coefficients in **Figure 9** are significant. The coefficient of the correlation ( $r$ ) between predicted and measured values are 0.863, following **Equation 4**, i.e., there is a strong correlation. Furthermore, the OLS regression between measured and predicted values also illustrates the significant relationship since

the slope is roughly 1.021 significantly, and the ideal value is 1. To confirm whether the goodness of fit of a specific year is apparently lower than other years', we calculate all the yearly statistical indicators. In **Table 1**, the yearly statistical indicators, including  $R^2$ , RMSE, correlation coefficient ( $r$ ), the slope and intercept of regressions between measured and predicted values, are listed. The lowest yearly  $R^2$  is 51.54% in 2021. The yearly RMSE and MAE peak in 2021 and 2018, respectively, which is 9.619 and 4.071  $\mu g/m^3$ . In September 2021, the measured ground-level  $NO_2$  concentration in Puebla, a Mexican city, suddenly increases to more than 20 times the usual level. In October 2021, the data of this city are missing. As we mentioned in the Materials section, this seemingly strange record also causes the high skewness of measured ground-level  $NO_2$  concentration distribution. The available daily data in that city are close to its monthly average value in September 2021. Thus, we keep that record in the analysis. However, if we ignore this individual record, the  $R^2$  in 2021 will reach 78.10%. Comparisons of monthly time series illustrate that the GWPR captures the monthly temporal variability accurately (**Figure 10**).

*Figure 9 is located here.*

*Table 1 is located here.*

*Figure 10 is located here.*

**Table 2** reports the results of 10-fold cross validation. The total data set is randomly divided into ten subsets. In every single cross validation, nine subsets are used to train the model. Then the reserved subset and the coefficients from the trained model are employed to predict the dependent variable. The performance of the GWPR based on FEM is stable in terms of goodness of prediction for the test subsets. The lowest accuracy of prediction for the test subset is 68.55%, and its RMSE, MEA, and coefficient ( $r$ ) of the correlation

between predicted and measured values are  $15.569 \mu\text{g}/\text{m}^3$ ,  $4.399 \mu\text{g}/\text{m}^3$ , and 0.627, respectively. The 10-fold cross validation results show the reliability of the GWPR model.

*Table 2 is located here.*

### ***Validation of the OK Interpolations***

**Table 3** illustrates the result of the leave-one-out cross validation of the coefficient and mean value interpolations. The worst performance of the OK method is from the interpolation of the mean value of measured ground-level  $\text{NO}_2$ , whose  $R^2$  is 34.50%, but its RMSE and MAE are not high, which are  $7.773$  and  $5.633 \mu\text{g}/\text{m}^3$ , respectively. For the low values of its RMSE and MAE, this interpolated grid data set is still acceptable. There is a new indicator named on point  $R^2$  in **Table 3**. This indicator is to depict how much the observed values change after interpolation. In the OK method, the spatial weight might not equal 1 when the distance between two points equals 0, i.e., they are overlapped. Hence, after OK interpolation, the predicted values from the imputed grid data set might differ slightly from the observed values. The on-point  $R^2$  indicates that none of the interpolations lose the accuracy more than 2%, and most of them only slash 0.1% accuracy.

*Table 3 is located here.*

### ***Prediction and Monthly Change Trends***

The accuracy of the predicted grid data set is 69.61%, and the RMSE and MAE are  $7.82$  and  $4.07 \mu\text{g}/\text{m}^3$ , respectively. Due to the slight change in the interpolation process, the accuracy in the final prediction is lower than the result of GWPR. **Figure 11**

demonstrates the relationship between predicted and measured ground-level NO<sub>2</sub> concentrations in the predicted grid data sets, and all coefficients in **Figure 11** are significant. The  $r$  is 0.838, lower than the  $r$  in the GWPR result (0.859). According to the tiny difference of all statistical indicators between the GWPR result and the grid data prediction result, the final prediction data are reasonable.

*Figure 8 is located here.*

**Figure 12** presents the average monthly ground-level NO<sub>2</sub> concentration. The result shows that ground-level NO<sub>2</sub> concentration in Asia is relatively higher than in other continents. Moreover, in western Asia, the ground-level NO<sub>2</sub> pollution is most severe. In most regions of Iran, Iraq, and Turkmenistan, the average values even exceed 100  $\mu\text{g}/\text{m}^3$ , much higher than WHO's ambient NO<sub>2</sub> concentration limits, which is an annual mean of 40  $\mu\text{g}/\text{m}^3$  in link with previous studies (Kasparoglu et al. 2018; Yousefian et al. 2020). Moreover, partial regions in northern China, India, Chile, Bolivia, South Africa, northern Italy, and the west coast of the United States are also severely polluted, tallying with previous research (Di et al. 2020; Kim et al. 2021; Zheng et al. 2019). Moreover, in **Figure 12**, we plot 110 main cities' average measured ground-level NO<sub>2</sub> concentration from January 2015 to October 2021. The measured values are consistent with our predictions. The map of average monthly ground-level NO<sub>2</sub> concentration without city points and monthly ground-level NO<sub>2</sub> concentration from January 2015 to October 2021 are shown in the **Supplementary Materials (Figures S1 – S83)**. **Figure 13** shows the average monthly TrCA of NO<sub>2</sub> concentration from January 2015 to October 2021. There are some differences between the two spatial distributions. As assumed, the relationship between the TrCA of NO<sub>2</sub> and the ground-level NO<sub>2</sub> spatially varies. Thus, the same amounts of NO<sub>2</sub>

in the troposphere might contribute disproportionally to the ground-level NO<sub>2</sub> concentration in the different places. **Figure 14** displays the monthly trends of the means of predicted ground-level NO<sub>2</sub> concentration in all the grids and the cities with the measurements. Both the mean values of all the global grids and the cities with measurements show downtrends. The monthly change trends of each grid and the means of all the global grids and the cities with measurements are estimated following **Equation 20**. The slope of the regression between the average ground-level NO<sub>2</sub> concentration of the cities and month order is -0.097 (95% confidence interval: -0.140 - -0.053, p-value < 0.1%), indicating a roughly 0.097 (95% CI: 0.053 – 0.140)  $\mu\text{g}/\text{m}^3$  decrease per month from January 2015 to October 2021. Moreover, the mean of all the grids decreases by about 0.066 (95% CI: 0.033 - 0.099)  $\mu\text{g}/\text{m}^3$  (p-value < 0.1%) per month. **Figure 15** illustrates the monthly change trends of each grid. All the values shown in **Figure 15** should be significant at the 0.1 level. **Figure 15** demonstrates that the ground-level NO<sub>2</sub> concentration is gradually decreasing in most regions. However, in the Red Sea region, Arabian Peninsula, Persian Gulf, the ground-level NO<sub>2</sub> concentration is increasing, even though there are already the most severely polluted areas. In addition, the changes in most places in India and Mexico also show an upward trend. In some areas of California and Nevada, the United States, the change trends are on the rise.

*Figures 12-15 are located here.*

## Discussion

We employ the GWPR model to examine the association of satellite-derived data with measured ground-level NO<sub>2</sub> concentrations from January 2015 to October 2017, among 530 cities. The accuracies of the GWPR (74.45%) and raster prediction (69.61%) exceed most previous studies about regional ground-level NO<sub>2</sub> concentration (Kim et al. 2021; Li et al. 2020; Qin et al. 2017). Our analysis provides the first example of the GWPR on an unbalanced panel data set. Our study predicts 82 monthly global ground-level NO<sub>2</sub> concentrations with 0.25-arc-degree spatial resolution from January 2015 to October 2021 (Shown in the **Supplementary Materials**). Also, our analysis demonstrates the monthly change trends of each grid.

In terms of accuracy, our study has made some improvements in the ground-level NO<sub>2</sub> concentration estimation based on the satellite data set. The accuracy of a study on ground-level NO<sub>2</sub> concentration over Central-Eastern China employing GTWR is 0.60, lower than our 0.70 (Qin et al. 2017). Additionally, its MEA is  $9.28 \mu\text{g}/\text{m}^3$ , while our MEA is  $5.633 \mu\text{g}/\text{m}^3$ . A research over the Wuhan urban agglomeration applying space-time neural networks obtains 0.69 accuracy and an  $8.29\text{-}\mu\text{g}/\text{m}^3$  RMSE, while our RMSE is  $7.82 \mu\text{g}/\text{m}^3$  (Li et al. 2020). Additionally, a study over Switzerland and northern Italy using machine learning technology provides a 59%-accuracy prediction, and its MEA is  $7.69 \mu\text{g}/\text{m}^3$  (Kim et al. 2021). However, these studies excel at either spatial or temporal resolution.

The spatial distribution and concentrations of the predictions are compared with previous studies. According to a study by Di et al., in the metropolitan areas of Michigan,

Illinois, Wisconsin, New England, Colorado, Nevada and California, the NO<sub>2</sub> pollution is harmful, higher than 25 PPB (Di et al. 2020). Our prediction is in line with this study since the ground-level NO<sub>2</sub> in those places is predicted around 40  $\mu\text{g}/\text{m}^3$  (Under an ambient pressure of 1 atmosphere and a temperature of 25 °C, 1 PPB NO<sub>2</sub> roughly equals 1.88  $\mu\text{g}/\text{m}^3$ ). Kasparoglu et al. put forward that in urban sites of Marmara regression of Turkey, the NO<sub>2</sub> concentration are higher than 75  $\mu\text{g}/\text{m}^3$  (Kasparoglu et al. 2018), consistent with our study. Yousefian et al. propose that during 2012 - 2017, the NO<sub>2</sub> concentration in Tehran, the Capital of Iran, is always 1.5 - 2.5 times higher than WHO limits (40  $\mu\text{g}/\text{m}^3$ ) (Yousefian et al. 2020), where is also the most polluted area in our research. Kim et al.'s research hints that in an Alpine domain, the NO<sub>2</sub> in the urban regions is always over 40  $\mu\text{g}/\text{m}^3$  (Kim et al. 2021), which is in keeping with our study. Additionally, Chi et al. estimate the annual average ground-level NO<sub>2</sub> concentration in the main regions of China over 2014 – 2020 (Chi et al. 2021). Its results are similar to our predictions. Moreover, because the research on the ground-level NO<sub>2</sub> concentration in polar regions is rare, it is difficult to compare our study with previous. However, the low temperature and PBLH might account for the high NO<sub>2</sub> concentration in polar regions. Evidence shows that in winter, the NO<sub>2</sub> concentration is apparently higher than it in summer (Fan et al. 2020; Shen et al. 2021; Yousefian et al. 2020). PBLH is negatively related to ground-level air pollution (Xiang et al. 2019). To summarize, our study is in line with the most recent studies on ground-level NO<sub>2</sub> concentration.

It must be underscored that the spatial distributions of ground-level NO<sub>2</sub> concentration and TrCA of NO<sub>2</sub> are different, as **Figures 12** and **13** shown. Putting another way, the impacts of the TrCA of NO<sub>2</sub> on the ground-level NO<sub>2</sub> concentration spatially

vary. **Figure 3.a** illustrates the discrepancy between the TrCA of NO<sub>2</sub> and the ground-level NO<sub>2</sub> concentration. For example, some points with no more than 1000  $\mu\text{g}/\text{m}^2$  TrCA of NO<sub>2</sub> have a more-than-60- $\mu\text{g}/\text{m}^3$  ground-level NO<sub>2</sub> concentration. The potential reason for this case is that most NO<sub>2</sub> in a certain column distributes near the surface, though the total amount of NO<sub>2</sub> in this column is rare. Moreover, several other points with more than 20000  $\mu\text{g}/\text{m}^2$  TrCA of NO<sub>2</sub> have a less-than-30- $\mu\text{g}/\text{m}^3$  ground-level NO<sub>2</sub> concentration. In this case, there is a large amount of NO<sub>2</sub> molecules in a specific column, but most of them might be hundreds of meters away from the surface. Several geoengineering measures could drive air pollution to penetrate the planetary boundary layer into the troposphere to avoid clustering at the surface (Liu et al. 2021). The ground-level atmospheric monitoring equipment cannot detect these NO<sub>2</sub> molecules, even though emissions might be high there. Because the physical and chemical properties of the atmosphere affected by geographical and environmental factors are not the same everywhere, we employ GWPR to predict the ground-level NO<sub>2</sub> concentration rather than use other global models to estimate it directly. The spatially varied relationship between the TrCA of NO<sub>2</sub> and the ground-level NO<sub>2</sub> concentration is the main reason leading to the difference between **Figures 12** and **13**.

Our monthly grid data demonstrate that the temporal variation of the spatial distribution of the ground-level NO<sub>2</sub> concentration is evident (Shown in **Supplementary Materials** and **Figure 10**). In December, January, and February, the NO<sub>2</sub> pollution over the Northern Hemisphere is relatively serious, while it is high in June, July, and August over the Southern Hemisphere. The possible reasons for this temporal variation are as follows: firstly, NO<sub>2</sub> can last longer, or it is difficult to be removed in a low-temperature



environment (Yousefian et al. 2020); secondly, residential energy for heating might produce more NO<sub>2</sub> (Fan et al. 2020); and thirdly, the low temperature changes other meteorological factors eventually leading to NO<sub>2</sub> unable to spread to other zones far from the surface (Fan et al. 2020; Shen et al. 2021). However, no matter which is the main reason, the policymakers should take this temporal variation into account in the air pollution policies.

However, some limitations remain in our study. Firstly, the number of measurement points is limited, and their spatial distribution is unbalanced. Our data set takes only 530 cities into account globally without rural areas. Especially in Africa and South America, there are few measurement points. Secondly, the spatial resolutions of one control variable, namely PBLH, are not good enough. Thirdly, some hidden variables are ignored. For instance, the research does not involve the impacts of air pollution policies and COVID-19, though we have used year dummy variables to reduce their effects. Fourthly, the spatial and temporal resolutions are relatively low. Future studies are better to focus on the following topics. Firstly, the GWPR model should be further optimized. For example, if the data set contains data islands based on a certain bandwidth, whether the GWRP is still statistically reliable remains unknown. Secondly, more confounders, such as land cover, human activity, among others, are needed in future analyses. Finally, the vertical distribution of NO<sub>2</sub> in air and its physical and chemical reasons are better to be carefully explored. Thirdly, the vertical distribution of air pollutants in the atmosphere in different places should be probed and analyzed.

## Conclusions

This study creates a GWPR model to detect the spatial variation of the relationship between the measured ground-level NO<sub>2</sub> concentration and satellite-derived data and predict the monthly ground-level NO<sub>2</sub> concentration based on the data from the OMI and other satellite platforms. The GWPR model illustrates the outstanding accuracy (0.7445), *r* value (0.863), RMSE (7.171  $\mu\text{g}/\text{m}^3$ ) and MAE (3.480  $\mu\text{g}/\text{m}^3$ ) in the estimation and stability in the cross validation. The GWPR is a simple but effective model to estimate monthly global ground-level NO<sub>2</sub> concentration at a 0.25-degree spatial resolution. The predictions provide critical basic data to environmental and public health science and valuable information for governments and societies to formulate more reasonable and efficient policies.

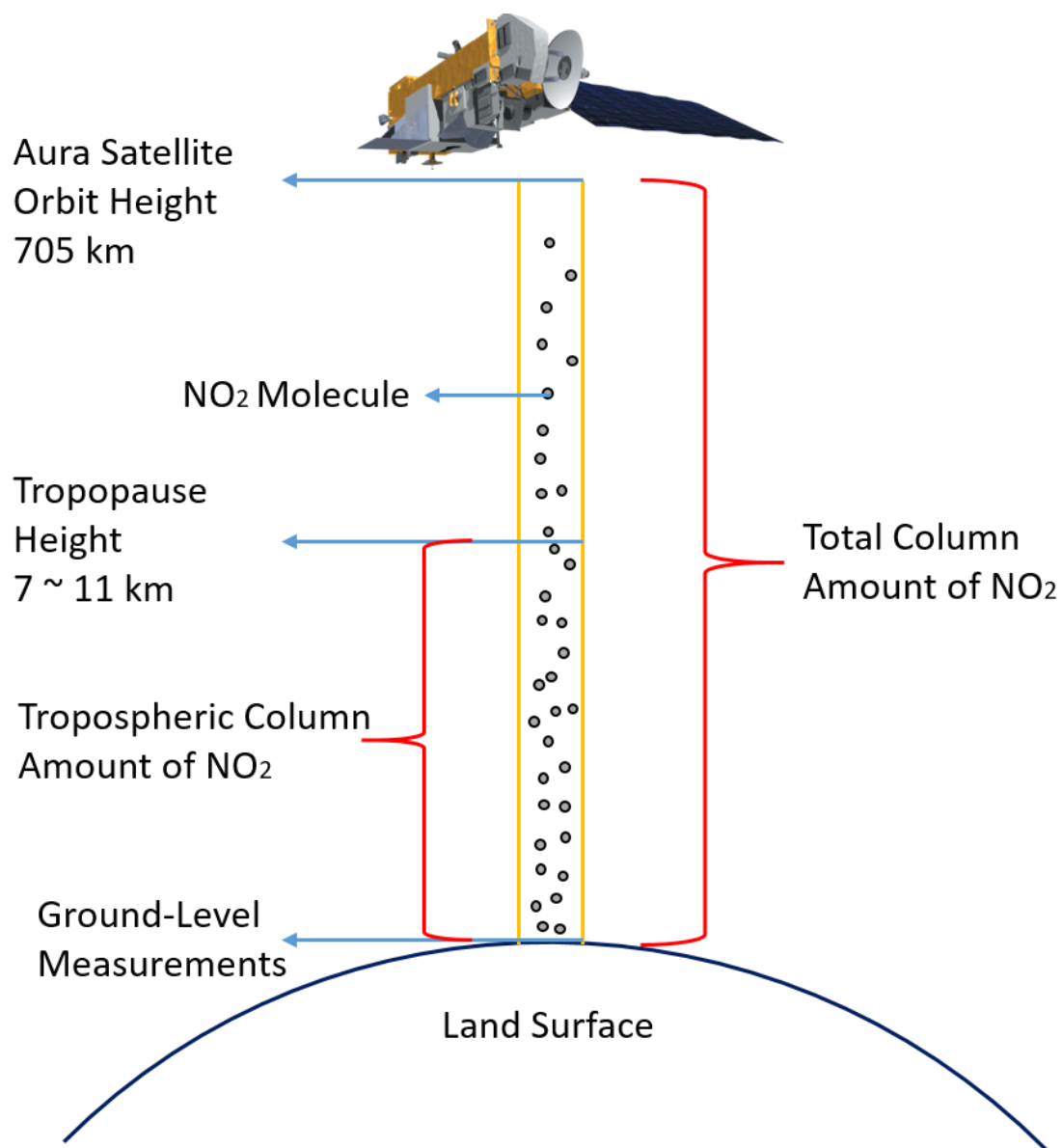
## Data Availability

All data sources used in the analyses, along with fully reproducible code, are publicly available at [https://github.com/MichaelChaoLi-cpu/Monthly\\_Global\\_Ground\\_Level\\_NO2](https://github.com/MichaelChaoLi-cpu/Monthly_Global_Ground_Level_NO2). The predicted data from January 2015 to October 2021 and the animation of ground-level NO<sub>2</sub> concentration could also be found in the abovementioned websites.

## Acknowledgments

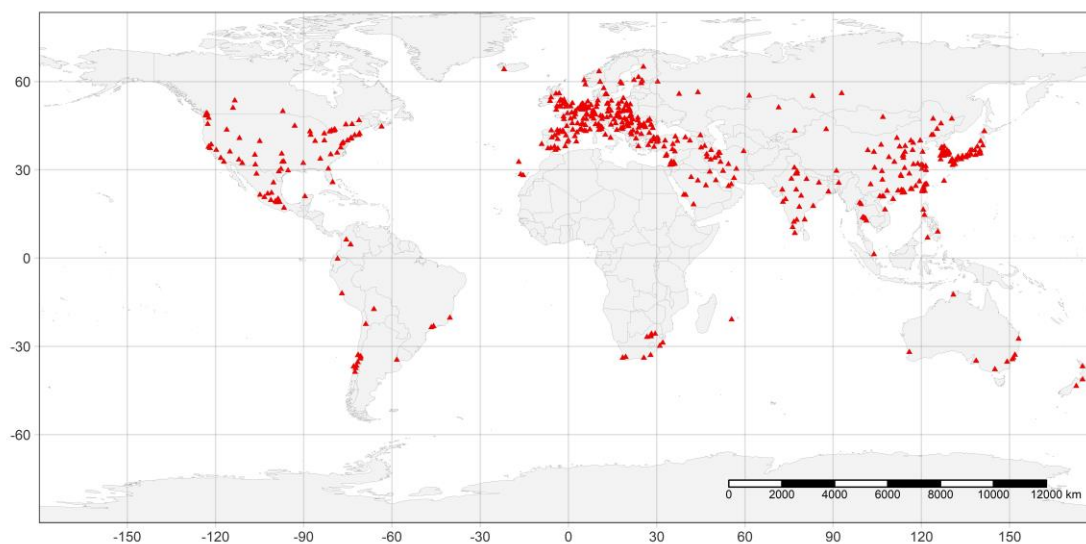
The authors gratefully acknowledge all the support, financial or otherwise, in enabling the work here to be carried out. This research was supported by the following funding agencies: JSPS KAKENHI (Grant No. JP20H00648), the Environment Research and Technology Development Fund of the Environmental Restoration and Conservation Agency of Japan (Grant No. JPMEERF20201001), and also JST SPRING (Grant No. JPMJSP2136).

737 **Figure**



738

739 **Figure 1: Illustration regarding TrCA, ToCA, and Ground-Level Measurements**



740

741

**Figure 2: Map of City Locations with the Measurement Points**

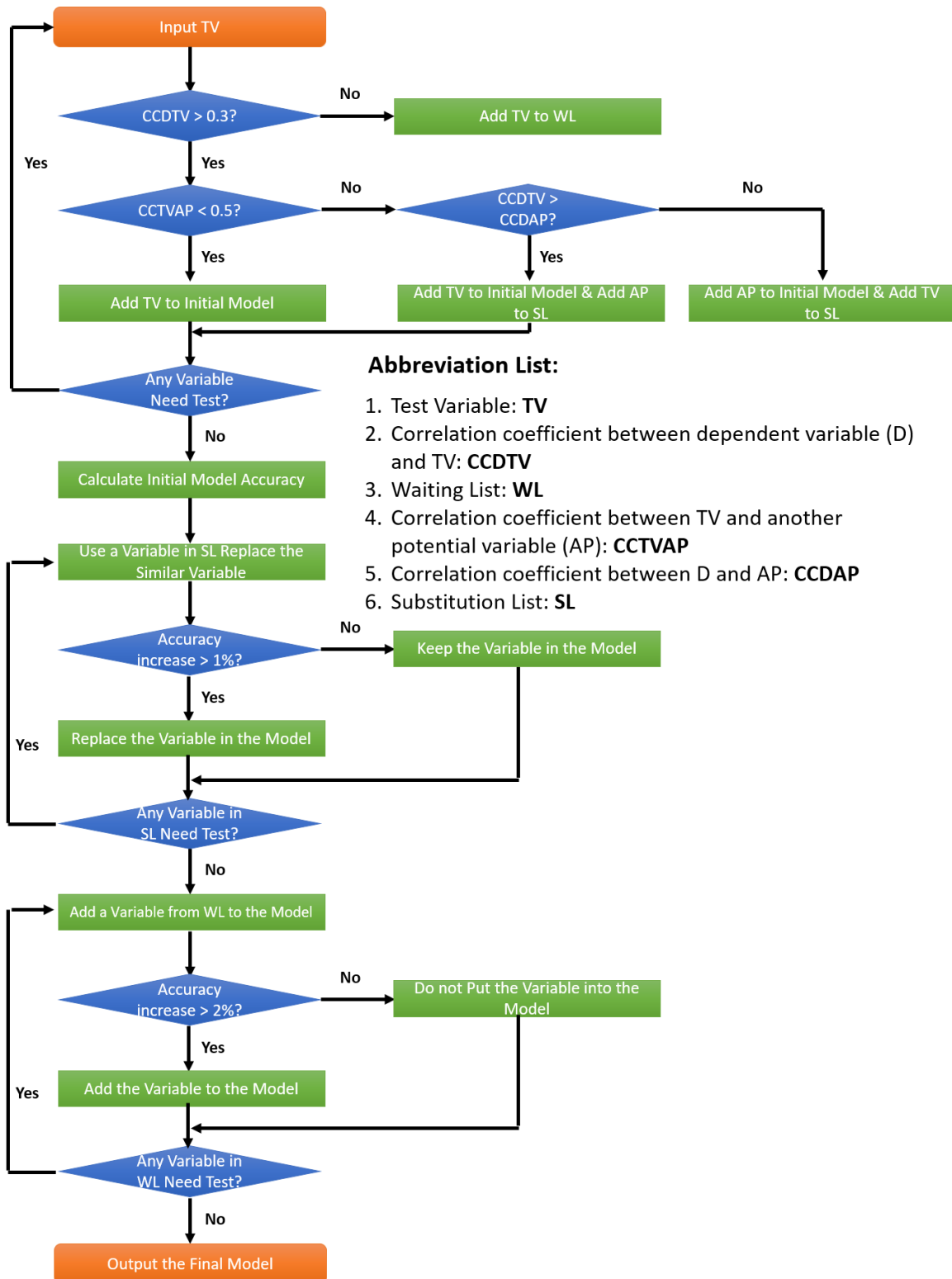


**Figure 3: Flow Chart of Variable Selection Process**

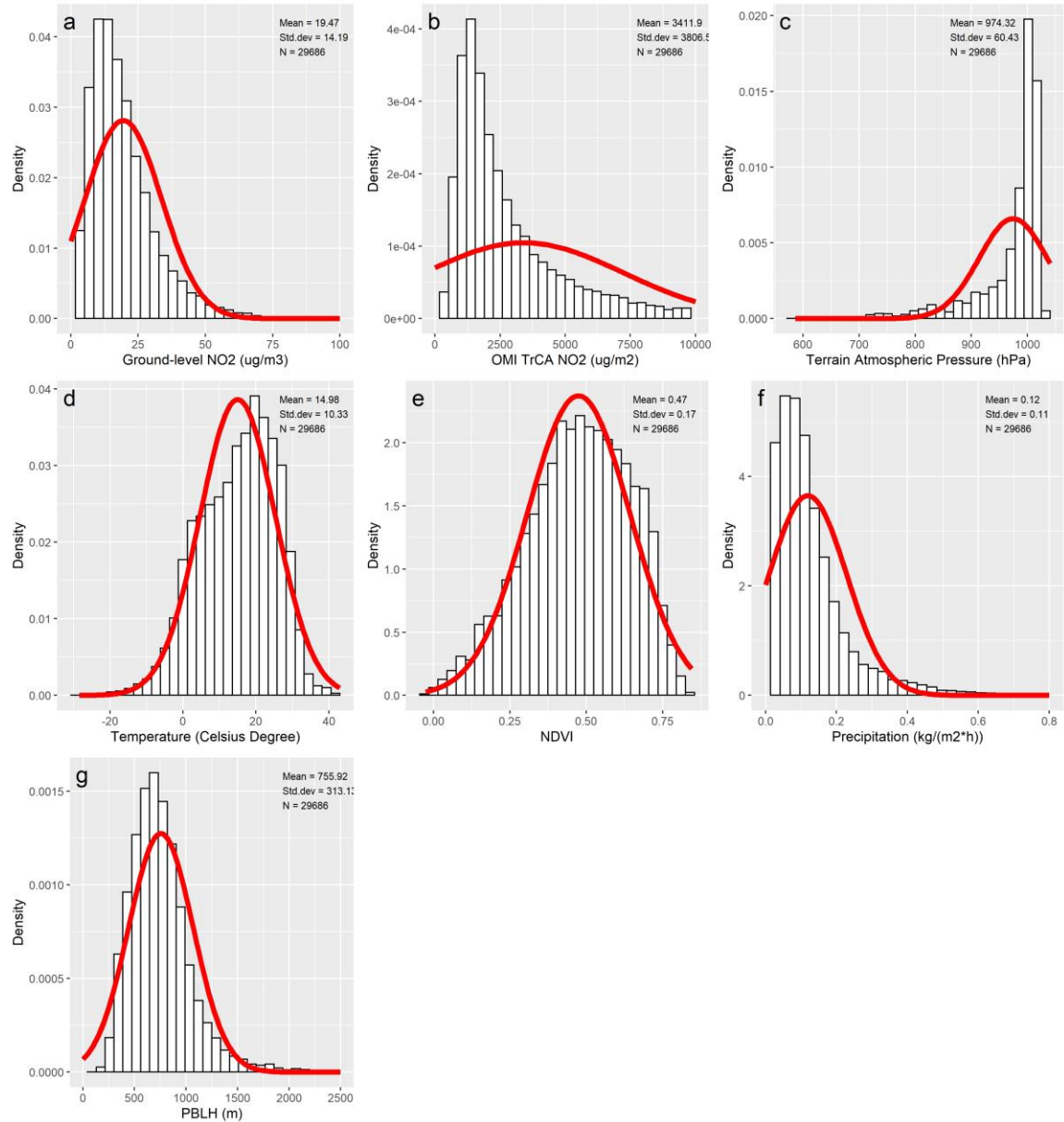


**Figure 4: Statistical Distributions and Descriptive Statistics of the Variables in the Original Data Set**

(The red line is the normal curve.)

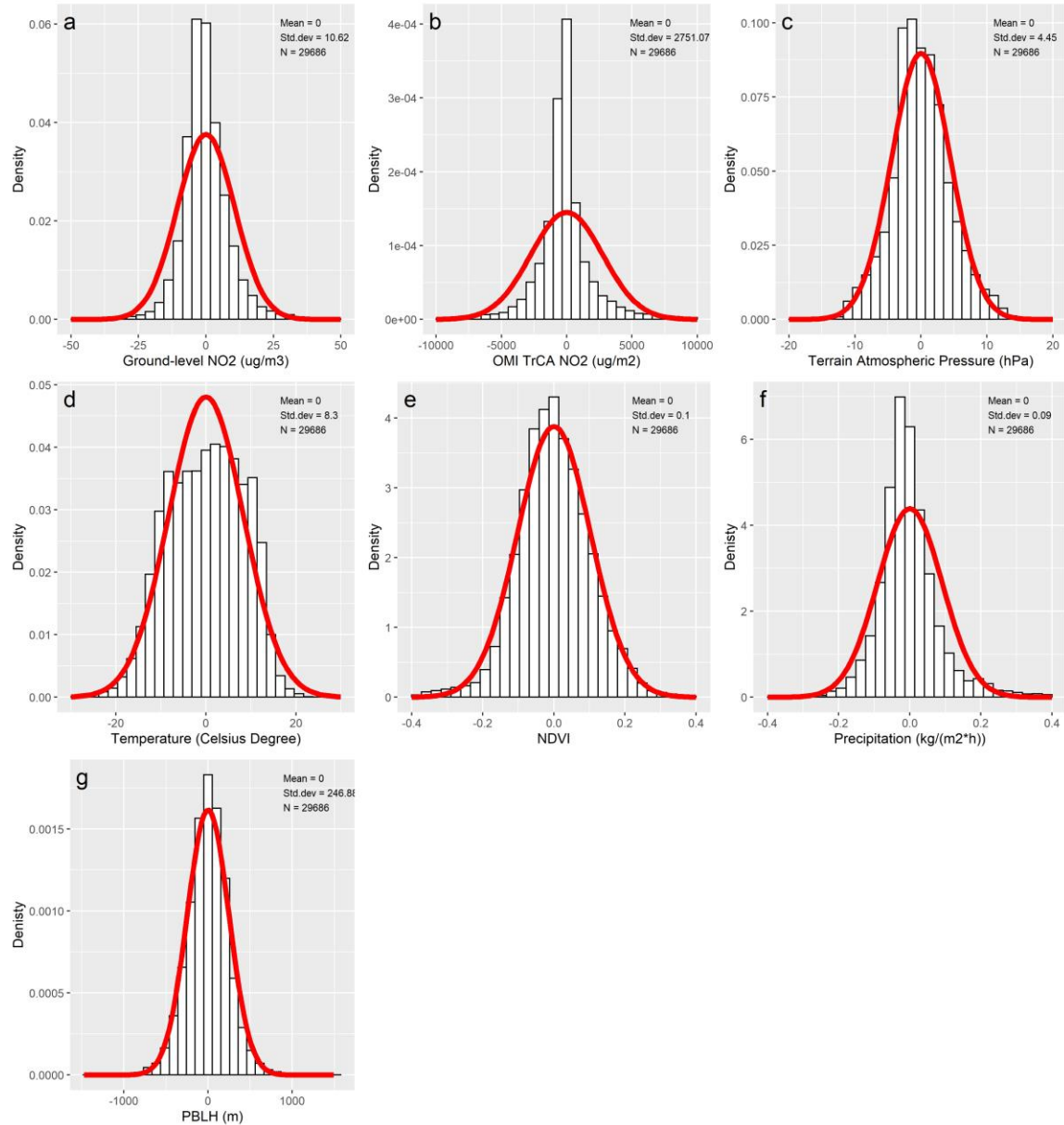


**Figure 5: Statistical Distributions and Descriptive Statistics of the Variables in the Transformed Data Set**

(The red line is the normal curve.)



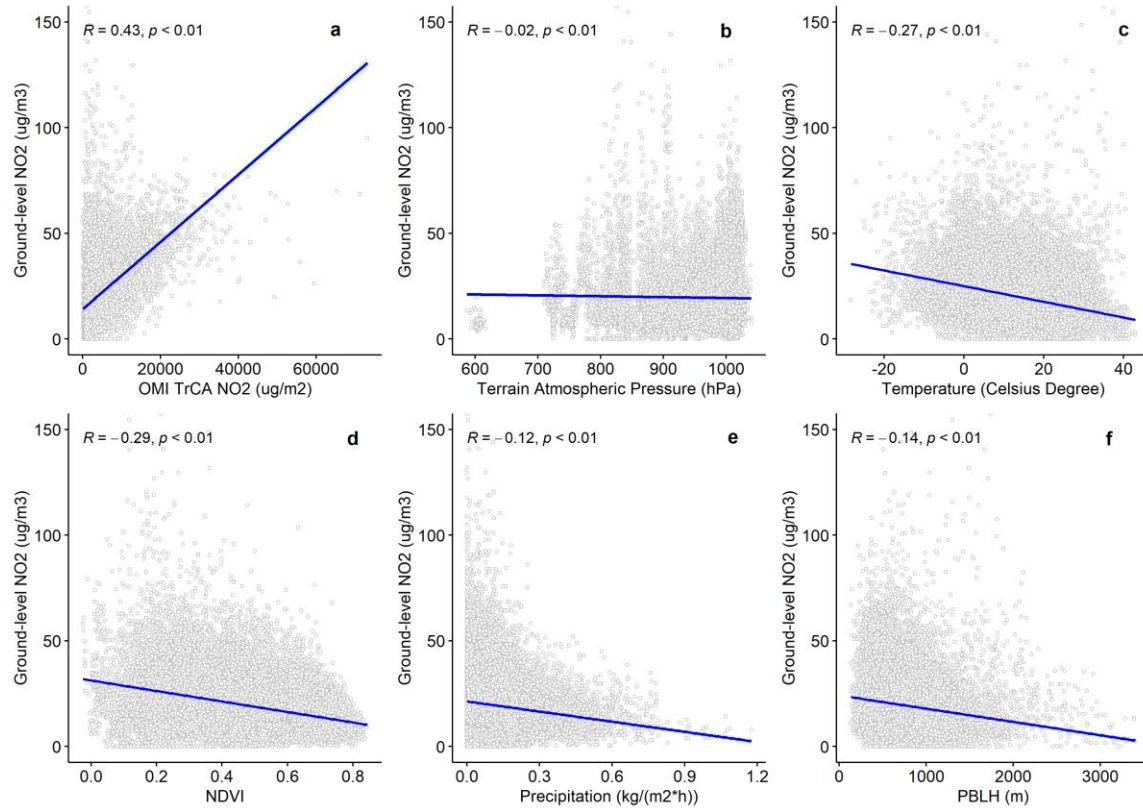


**Figure 6: Linear Trends and Correlation Coefficients between Variables in the Original Data Set**

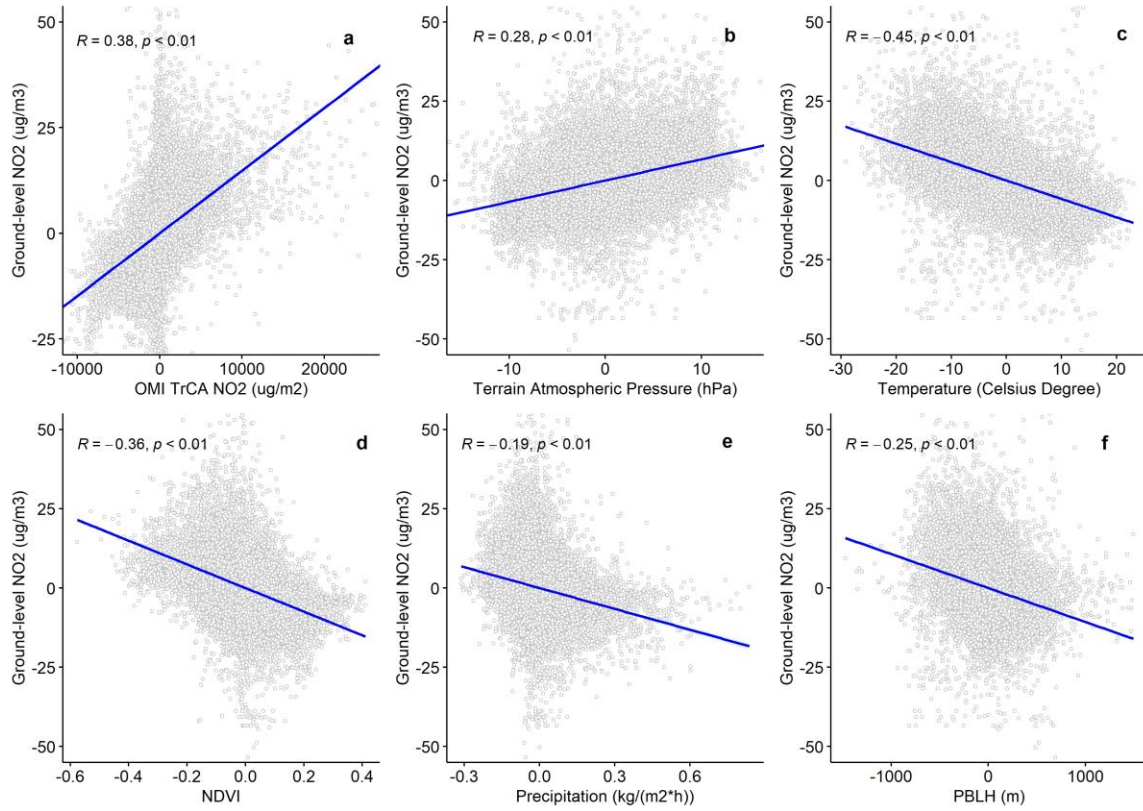


**Figure 7: Linear Trends and Correlation Coefficients between Variables in the Transformed Data Set**

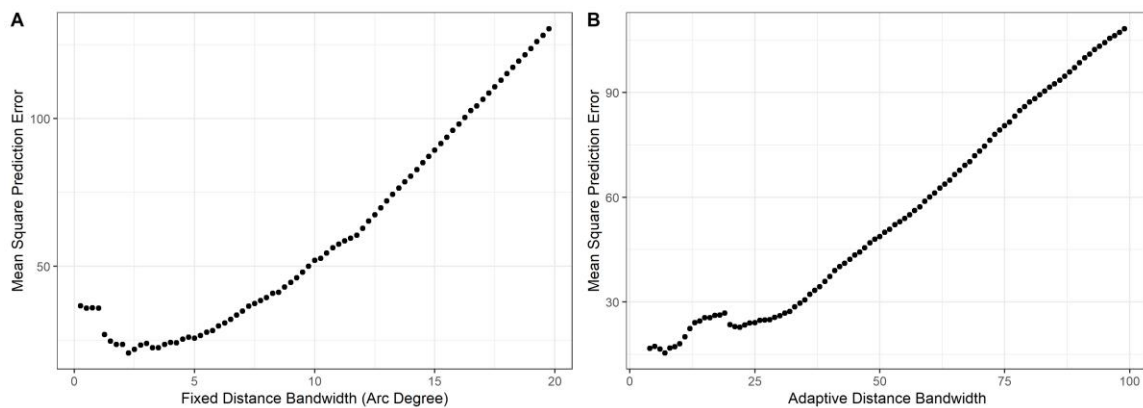


**Figure 8: Step Increment Bandwidth Selection**

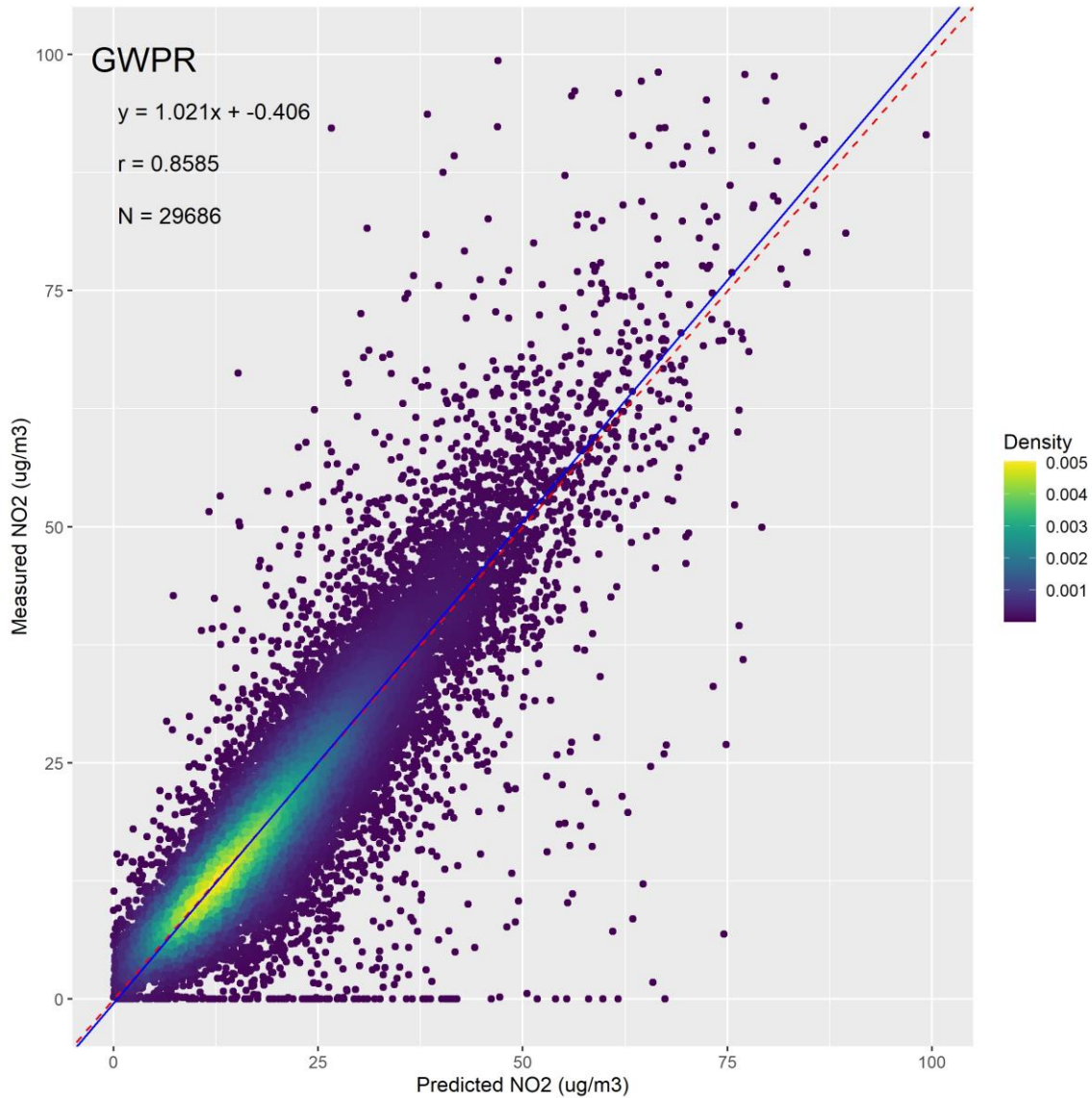


**Figure 9: The Density Plots between the Measured Ground-Level NO<sub>2</sub> Concentration and the Predicted NO<sub>2</sub> Concentration from the GWPR Result.**

(The red dashed line is the 1:1 line. The blue line is the regression line.)

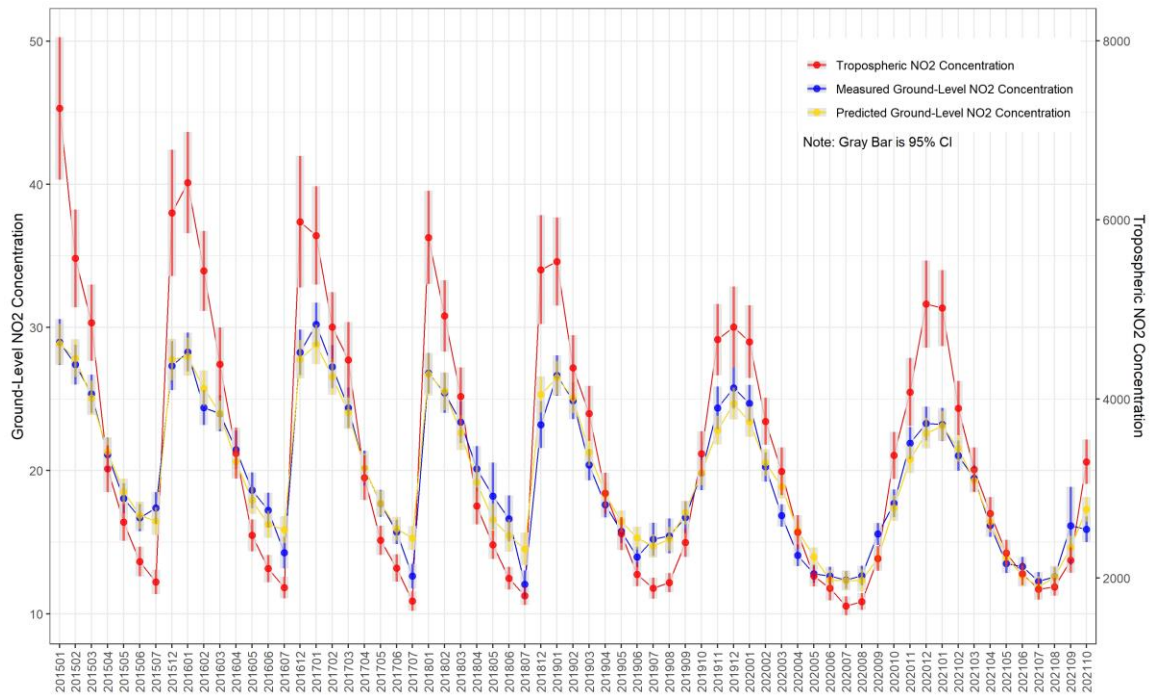
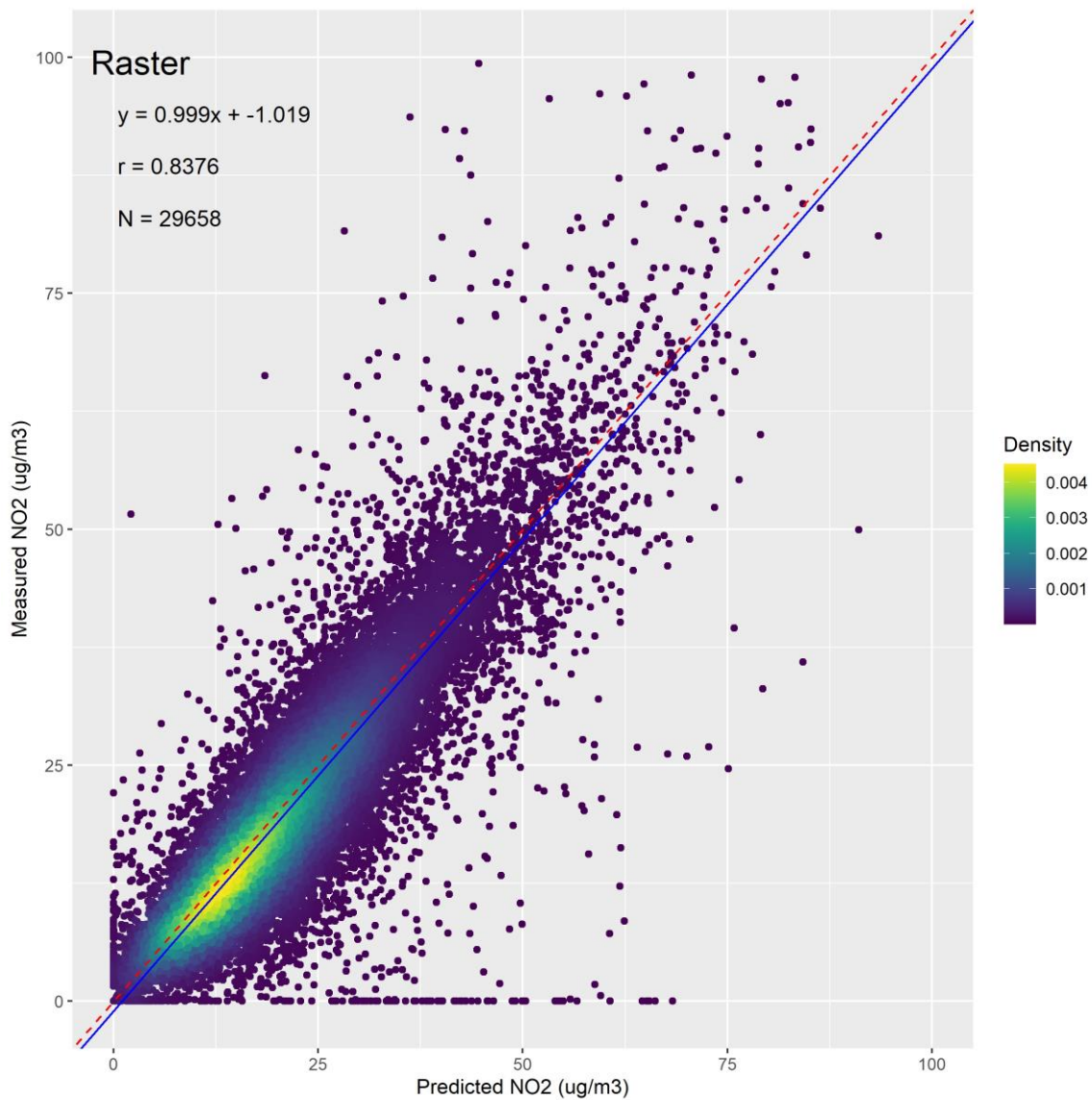


**Figure 10: Time Series Comparisons of Monthly Means of Tropospheric, Measured Ground-Level, Predicted Ground-Level NO<sub>2</sub> Concentration and Their 95% Confidence Interval**  
(Unit: Tropospheric NO<sub>2</sub> Concentration [ $\mu\text{g}/\text{m}^2$ ], Measured and Predicted Ground-Level NO<sub>2</sub> Concentration [ $\mu\text{g}/\text{m}^3$ ])

778



779

780

781

782

783

784

**Figure 11: The Density Plots between the Measured Ground-Level NO<sub>2</sub> Concentration and the Predicted NO<sub>2</sub> Concentration from the Predicted Grid Data Sets.**

(The red dashed line is the 1:1 line. The blue line is the regression line.)





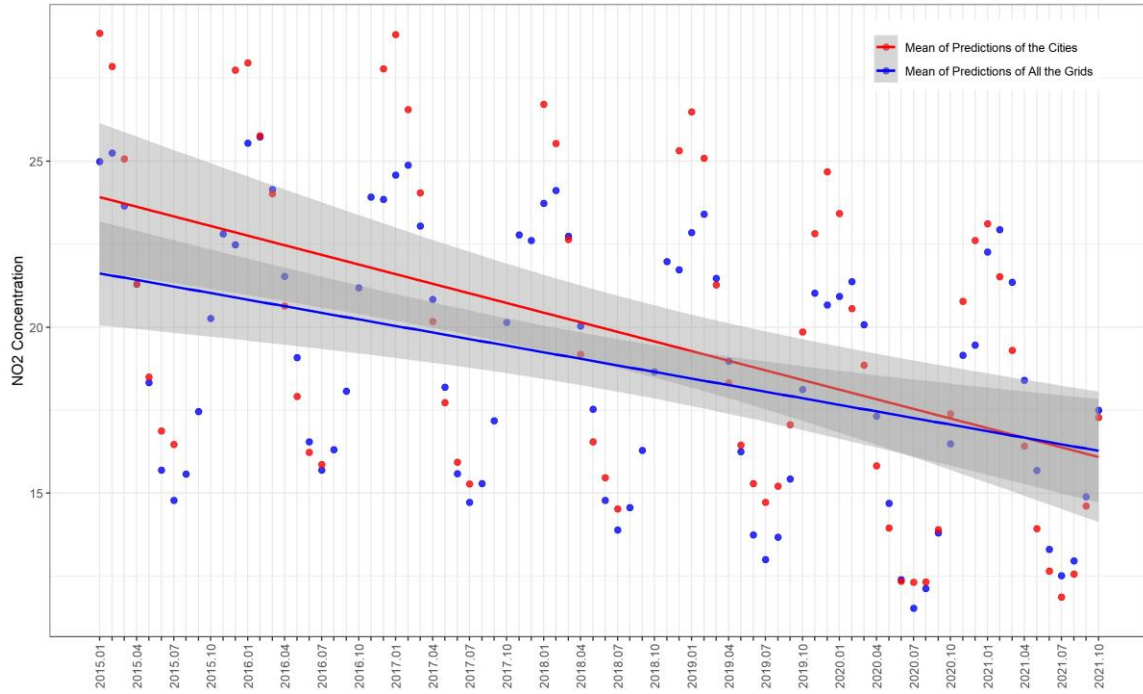


**Figure 14: Monthly Change Trends of Average Predicted Ground-Level NO<sub>2</sub> Concentration ( $\mu\text{g}/\text{m}^3$ ), Jan 2015 – Oct 2021**

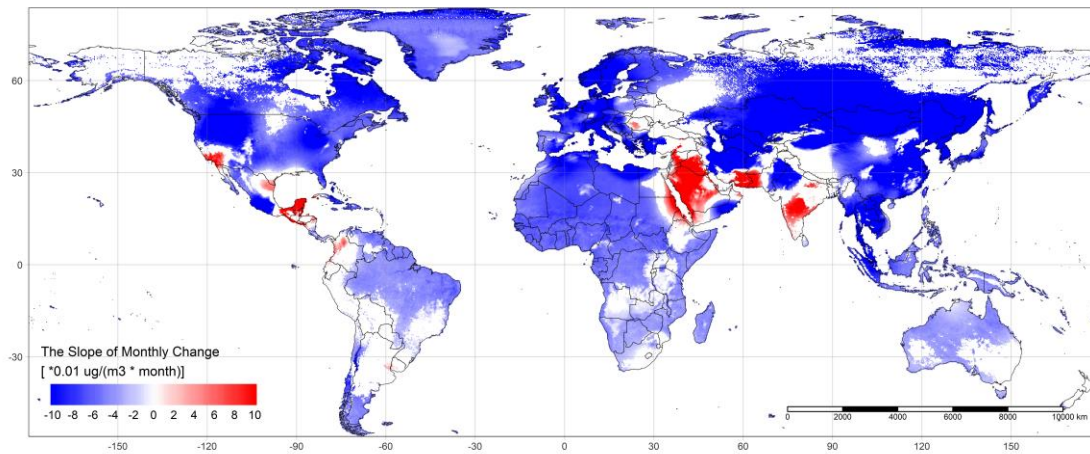


**Figure 15: Map of Monthly Change Trends of Ground-Level NO<sub>2</sub> Concentration ( $0.01 \mu\text{g}/(\text{m}^3 \times \text{month})$ ), Jan 2015 – Oct 2021**

801 **Table**

**Table 1: Yearly Statistical Indicators Summary of the GWPR Results**

Year	N	R <sup>2</sup>	RMSE ( $\mu\text{g}/\text{m}^3$ )	MAE ( $\mu\text{g}/\text{m}^3$ )	r	Slope	Intercept
2015	3115	86.46%	5.151	3.476	0.930	0.843	3.623
2016	3315	81.64%	6.126	3.617	0.904	0.794	4.508
2017	2936	85.20%	5.442	3.355	0.925	0.803	4.242
2018	3560	74.99%	8.881	4.071	0.869	0.689	6.461
2019	5790	71.34%	7.475	3.566	0.846	0.676	6.418
2020	6023	77.32%	5.317	3.335	0.881	0.827	2.912
2021	4947	51.55%	9.619	3.115	0.718	0.520	7.831
Total	29686	74.45%	7.171	3.480	0.863	0.724	5.373

Note: The Ideal value of slope is 1, and the ideal value of intercept is 0.

802

**Table 2: Statistical Indicators Summary of 10-Fold Cross Validation**

Statistical Indicator of Training								Statistical Indicator of Testing						
N	R2	RMSE $\mu\text{g}/\text{m}^3$	MAE $\mu\text{g}/\text{m}^3$	r	Slope	Intercep t		N	R2	RMSE $\mu\text{g}/\text{m}^3$	MEA $\mu\text{g}/\text{m}^3$	r	Slope	Intercep t
1	26718	89.68%	7.746	3.800	0.839	0.681	6.195	2968	89.73%	7.669	4.096	0.831	0.691	6.139
2	26718	89.47%	7.843	3.861	0.837	0.684	6.151	2968	89.90%	7.422	4.367	0.825	0.733	5.296
3	26718	89.54%	7.828	3.846	0.839	0.683	6.148	2968	91.42%	6.754	3.994	0.844	0.799	4.160
4	26718	92.53%	6.464	3.719	0.876	0.749	4.926	2968	68.55%	15.57	4.399	0.627	0.358	12.275
5	26718	89.96%	7.640	3.763	0.844	0.692	6.009	2968	91.02%	7.155	4.055	0.854	0.711	5.592
6	26718	90.04%	7.637	3.828	0.847	0.694	5.960	2968	90.13%	7.267	4.025	0.826	0.793	4.044
7	26718	89.61%	7.777	3.790	0.839	0.681	6.226	2968	92.39%	6.546	3.997	0.875	0.762	4.511
8	26718	90.55%	7.404	3.724	0.853	0.705	5.756	2968	89.39%	7.875	4.171	0.834	0.683	6.137
9	26718	90.95%	7.268	3.742	0.862	0.712	5.602	2968	89.98%	7.418	4.160	0.828	0.781	4.391
10	26712	90.27%	7.515	3.759	0.849	0.693	5.976	2974	90.76%	7.332	4.086	0.856	0.710	5.718

Note: The Ideal value of slope is 1, and the ideal value of intercept is 0. When the values of statistical indicators are close between training results and testing result, the predictions of model are reliable.

803

804



**Table 3: Statistical Indicators Summary of the Leave-One-Out Cross Validation of OK Interpolation**

	Variable	N	R <sup>2</sup>	MRSE $\mu g/m^3$	MAE $\mu g/m^3$	r	Intercept	Slope	On Point R <sup>2</sup>
Coefficient Interpolation	TrCA of NO <sub>2</sub> Terrain	530	67.54%	8.49E-04	3.81E-04	0.826	-9.31E-05	1.109	99.87%
	Atmospheric Pressure	530	77.99%	0.148	0.079	0.883	0.003	1.021	99.86%
	Temperature	530	60.11%	0.320	0.102	0.778	0.015	1.080	99.91%
	NDVI	530	79.28%	16.815	6.491	0.892	1.065	1.053	99.93%
	Precipitation	530	75.46%	14.210	5.288	0.869	0.682	1.037	99.91%
	PBLH	530	72.38%	0.004	0.002	0.852	0.001	1.054	99.83%
	2016 Year	530	72.38%	0.004	0.002	0.852	0.001	1.054	99.85%
	2017 Year	530	71.89%	3.161	1.378	0.848	0.081	1.021	99.87%
	2018 Year	530	55.09%	6.727	1.986	0.743	0.218	1.009	99.83%
	2019 Year	530	72.50%	3.642	1.555	0.852	0.150	1.028	99.87%
	2020 Year	530	75.28%	3.273	1.443	0.868	0.170	1.013	99.87%
	2021 Year	530	76.82%	3.791	1.643	0.877	0.223	1.029	99.87%
Mean Value Interpolation	Measured Ground- Level NO <sub>2</sub>	530	34.50%	7.773	5.633	0.626	4.505	0.748	98.40%
	TrCA of NO <sub>2</sub> Terrain	530	79.85%	1143.454	738.228	0.896	75.632	0.946	99.59%
	Atmospheric Pressure	530	67.70%	36.269	21.535	0.823	-17.663	1.018	99.79%
	Temperature	530	84.21%	2.597	1.564	0.919	-0.821	1.046	99.92%
	NDVI	530	54.86%	0.095	0.068	0.748	0.059	0.876	99.44%
	Precipitation	530	86.86%	0.022	0.012	0.932	-0.002	1.009	99.94%
	PBLH	530	77.98%	101.276	53.343	0.883	-18.025	1.024	99.91%

805

806

807

## 808 Reference:

- 809 Bechle, M.J., Millet, D.B., & Marshall, J.D. (2015). National Spatiotemporal Exposure  
810 Surface for NO<sub>2</sub>: Monthly Scaling of a Satellite-Derived Land-Use Regression, 2000–  
811 2010. *Environmental Science & Technology*, 49, 12297-12305
- 812 Beckerman, B., Jerrett, M., Brook, J.R., Verma, D.K., Arain, M.A., & Finkelstein, M.M.  
813 (2008). Correlation of nitrogen dioxide with other traffic pollutants near a major  
814 expressway. *Atmospheric Environment*, 42, 275-290
- 815 Beenstock, M., & Felsenstein, D. (2019). *The econometric analysis of non-stationary*  
816 *spatial panel data*. Springer
- 817 Bigdeli, M., Taheri, M., & Mohammadian, A. (2021). Spatial sensitivity analysis of  
818 COVID-19 infections concerning the satellite-based four air pollutants levels.  
819 *International Journal of Environmental Science and Technology*, 18, 751-760
- 820 Breusch, T.S., & Pagan, A.R. (1980). The Lagrange Multiplier Test and its Applications to  
821 Model Specification in Econometrics. *The Review of Economic Studies*, 47, 239
- 822 Brunekreef, B., & Holgate, S.T. (2002). Air pollution and health. *The Lancet*, 360, 1233-  
823 1242
- 824 Brunsdon, C., Fotheringham, A.S., & Charlton, M.E. (2010). Geographically Weighted  
825 Regression: A Method for Exploring Spatial Nonstationarity. *Geographical Analysis*, 28,  
826 281-298
- 827 Brunsdon, C., Fotheringham, S., & Charlton, M. (1998). Geographically Weighted  
828 Regression. *Journal of the Royal Statistical Society: Series D (The Statistician)*, 47, 431-  
829 443
- 830 Chang, Y., Wang, S., Zhou, Y., Wang, L., & Wang, F. (2019). A Novel Method of  
831 Evaluating Highway Traffic Prosperity Based on Nighttime Light Remote Sensing. *Remote*  
832 *Sensing*, 12, 102
- 833 Chi, Y., Fan, M., Zhao, C., Sun, L., Yang, Y., Yang, X., & Tao, J. (2021). Ground-level  
834 NO<sub>2</sub> concentration estimation based on OMI tropospheric NO<sub>2</sub> and its spatiotemporal  
835 characteristics in typical regions of China. *Atmospheric Research*, 264, 105821
- 836 Chiusolo, M., Cadum, E., Stafoggia, M., Galassi, C., Berti, G., Faustini, A., Bisanti, L.,  
837 Vigotti, M.A., Dessì M.P., Cernigliaro, A., Mallone, S., Pacelli, B., Minerba, S., Simonato,  
838 L., & Forastiere, F. (2011). Short-Term Effects of Nitrogen Dioxide on Mortality and  
839 Susceptibility Factors in 10 Italian Cities: The EpiAir Study. *Environmental Health*  
840 *Perspectives*, 119, 1233-1238
- 841 Croissant, Y., & Millo, G. (2008). Panel Data Econometrics in R: The plm Package.  
842 *Journal of Statistical Software*, 27
- 843 Curier, R.L., Kranenburg, R., Segers, A.J.S., Timmermans, R.M.A., & Schaap, M. (2014).  
844 Synergistic use of OMI NO<sub>2</sub> tropospheric columns and LOTOS–EUROS to evaluate the  
845 NO<sub>x</sub> emission trends across Europe. *Remote Sensing of Environment*, 149, 58-69
- 846 Di, Q., Amini, H., Shi, L., Kloog, I., Silvern, R., Kelly, J., Sabath, M.B., Choirat, C.,  
847 Koutrakis, P., Lyapustin, A., Wang, Y., Mickley, L.J., & Schwartz, J. (2020). Assessing  
848 NO<sub>2</sub> Concentration and Model Uncertainty with High Spatiotemporal Resolution across  
849 the Contiguous United States Using Ensemble Model Averaging. *Environmental Science*  
850 *& Technology*, 54, 1372-1384

851 Fan, H., Zhao, C., & Yang, Y. (2020). A comprehensive analysis of the spatio-temporal  
 852 variation of urban air pollution in China during 2014–2018. *Atmospheric Environment*, 220,  
 853 117066  
 854 Fotheringham, A., Brunson, C., & Charlton, M. (2002). *Geographically Weighted*  
 855 *Regression: The Analysis of Spatially Varying Relationships*. John Wiley & Sons  
 856 Fotheringham, A.S., Crespo, R., & Yao, J. (2015). Geographical and Temporal Weighted  
 857 Regression (GTWR). *Geographical Analysis*, 47, 431-452  
 858 Fotheringham, A.S., & Oshan, T.M. (2016). Geographically weighted regression and  
 859 multicollinearity: dispelling the myth. *Journal of Geographical Systems*, 18, 303-329  
 860 Geddes, J.A., Martin, R.V., Boys, B.L., & Van Donkelaar, A. (2016). Long-Term Trends  
 861 Worldwide in Ambient NO<sub>2</sub> Concentrations Inferred from Satellite Observations.  
 862 *Environmental Health Perspectives*, 124, 281-289  
 863 Gollini, I., Lu, B., Charlton, M., Brunson, C., & Harris, P. (2015). GWmodel: An R  
 864 package for exploring spatial heterogeneity using geographically weighted models.  
 865 *Journal of Statistical Software*, 63  
 866 Hamra, G.B., Laden, F., Cohen, A.J., Raaschou-Nielsen, O., Brauer, M., & Loomis, D.  
 867 (2015). Lung Cancer and Exposure to Nitrogen Dioxide and Traffic: A Systematic Review  
 868 and Meta-Analysis. *Environmental Health Perspectives*, 123, 1107-1112  
 869 Hu, X., Waller, L.A., Al-Hamdan, M.Z., Crosson, W.L., Estes, M.G., Estes, S.M.,  
 870 Quattrochi, D.A., Sarnat, J.A., & Liu, Y. (2013). Estimating ground-level PM<sub>2.5</sub>  
 871 concentrations in the southeastern U.S. using geographically weighted regression.  
 872 *Environmental Research*, 121, 1-10  
 873 Irie, H., Boersma, K.F., Kanaya, Y., Takashima, H., Pan, X., & Wang, Z.F. (2012).  
 874 Quantitative bias estimates for tropospheric NO<sub>2</sub> columns retrieved from SCIAMACHY,  
 875 OMI, and GOME-2 using a common standard for East Asia. *Atmospheric Measurement*  
 876 *Techniques*, 5, 2403-2411  
 877 Jiang, M., Sun, W., Yang, G., & Zhang, D. (2017). Modelling Seasonal GWR of Daily  
 878 PM<sub>2.5</sub> with Proper Auxiliary Variables for the Yangtze River Delta. *Remote Sensing*, 9,  
 879 346  
 880 Kang, S. (1985). A note on the equivalence of specification tests in the two-factor  
 881 multivariate variance components model. *Journal of Econometrics*, 28, 193-203  
 882 Kasparoglu, S., Incecik, S., & Topcu, S. (2018). Spatial and temporal variation of O<sub>3</sub>, NO  
 883 and NO<sub>2</sub> concentrations at rural and urban sites in Marmara Region of Turkey.  
 884 *Atmospheric Pollution Research*, 9, 1009-1020  
 885 Kim, M., Brunner, D., & Kuhlmann, G. (2021). Importance of satellite observations for  
 886 high-resolution mapping of near-surface NO<sub>2</sub> by machine learning. *Remote Sensing of*  
 887 *Environment*, 264, 112573  
 888 Larkin, A., Geddes, J.A., Martin, R.V., Xiao, Q., Liu, Y., Marshall, J.D., Brauer, M., &  
 889 Hystad, P. (2017). Global Land Use Regression Model for Nitrogen Dioxide Air Pollution.  
 890 *Environmental Science & Technology*, 51, 6957-6964  
 891 Lelieveld, J., Evans, J.S., Fnais, M., Giannadaki, D., & Pozzer, A. (2015). The contribution  
 892 of outdoor air pollution sources to premature mortality on a global scale. *Nature*, 525, 367-  
 893 371  
 894 Li, C., & Managi, S. (2021a). Contribution of on-road transportation to PM<sub>2.5</sub>. *Scientific*  
 895 *Reports*, 11, 21320

896 Li, C., & Managi, S. (2021b). Spatial Variability of the Relationship between Air Pollution  
897 and Well-being. *Sustainable Cities and Society*, 103447

898 Li, C., & Managi, S. (2022). Impacts of air pollution on COVID-19 case fatality rate: a  
899 global analysis. *Environmental Science and Pollution Research*, Jan 4:1–14.

900 Li, J., & Heap, A.D. (2011). A review of comparative studies of spatial interpolation  
901 methods in environmental sciences: Performance and impact factors. *Ecological*  
902 *Informatics*, 6, 228-241

903 Li, L., & Wu, J. (2021). Spatiotemporal estimation of satellite-borne and ground-level NO<sub>2</sub>  
904 using full residual deep networks. *Remote Sensing of Environment*, 254, 112257

905 Li, T., Wang, Y., & Yuan, Q. (2020). Remote Sensing Estimation of Regional NO<sub>2</sub> via  
906 Space-Time Neural Networks. *Remote Sensing*, 12, 2514

907 Lin, C.-A., Chen, Y.-C., Liu, C.-Y., Chen, W.-T., Seinfeld, J.H., & Chou, C.C.K. (2019).  
908 Satellite-Derived Correlation of SO<sub>2</sub>, NO<sub>2</sub>, and Aerosol Optical Depth with  
909 Meteorological Conditions over East Asia from 2005 to 2015. *Remote Sensing*, 11, 1738

910 Liu, L., Zhang, X., Xu, W., Liu, X., Lu, X., Chen, D., Zhang, X., Wang, S., & Zhang, W.  
911 (2017). Estimation of monthly bulk nitrate deposition in China based on satellite NO<sub>2</sub>  
912 measurement by the Ozone Monitoring Instrument. *Remote Sensing of Environment*, 199,  
913 93-106

914 Liu, Y., Ming, T., Peng, C., Wu, Y., Li, W., De Richter, R., & Zhou, N. (2021). Mitigating  
915 air pollution strategies based on solar chimneys. *Solar Energy*, 218, 11-27

916 Mackerron, G., & Mourato, S. (2009). Life satisfaction and air quality in London.  
917 *Ecological Economics*, 68, 1441-1453

918 Meng, L., Liu, J., Tarasick David, W., Randel William, J., Steiner Andrea, K., Wilhelmsen,  
919 H., Wang, L., & Haimberger, L. (2021). Continuous rise of the tropopause in the Northern  
920 Hemisphere over 1980–2020. *Science Advances*, 7, eabi8065

921 Newell, K., Kartsonaki, C., Lam, K.B.H., & Kurmi, O.P. (2017). Cardiorespiratory health  
922 effects of particulate ambient air pollution exposure in low-income and middle-income  
923 countries: a systematic review and meta-analysis. *The Lancet Planetary Health*, 1, e368-  
924 e380

925 Nickolay, K., Lok, L., Sergey, M., Edward, C., Eric, B., William, S., Joanna, J., & the OMI  
926 core team (2019). OMI/Aura NO<sub>2</sub> Total and Tropospheric Column Daily L2 Global  
927 Gridded 0.25 degree x 0.25 degree V3. In N.G.S.F. Center (Ed.): Goddard Earth Sciences  
928 Data and Information Services Center (GES DISC)

929 Ogen, Y. (2020). Assessing nitrogen dioxide (NO<sub>2</sub>) levels as a contributing factor to  
930 coronavirus (COVID-19) fatality. *Science of The Total Environment*, 726, 138605

931 OMI Team (2012). Ozone Monitoring Instrument (OMI) data user's guide. In  
932 Orellano, P., Reynoso, J., Quaranta, N., Bardach, A., & Ciapponi, A. (2020). Short-term  
933 exposure to particulate matter (PM<sub>10</sub> and PM<sub>2.5</sub>), nitrogen dioxide (NO<sub>2</sub>), and ozone (O<sub>3</sub>)  
934 and all-cause and cause-specific mortality: Systematic review and meta-analysis.  
935 *Environment International*, 142, 105876

936 Pebesma, E.J. (2004). Multivariable geostatistics in S: the gstat package. *Computers &*  
937 *Geosciences*, 30, 683-691

938 Qin, K., Rao, L., Xu, J., Bai, Y., Zou, J., Hao, N., Li, S., & Yu, C. (2017). Estimating  
939 Ground Level NO<sub>2</sub> Concentrations over Central-Eastern China Using a Satellite-Based  
940 Geographically and Temporally Weighted Regression Model. *Remote Sensing*, 9, 950

Rice, M.B., Ljungman, P.L., Wilker, E.H., Gold, D.R., Schwartz, J.D., Koutrakis, P., Washko, G.R., O'Connor, G.T., & Mittleman, M.A. (2013). Short-Term Exposure to Air Pollution and Lung Function in the Framingham Heart Study. *American Journal of Respiratory and Critical Care Medicine*, 188, 1351-1357

Schoeberl, M.R., Douglass, A.R., Hilsenrath, E., Bhartia, P.K., Beer, R., Waters, J.W., Gunson, M.R., Froidevaux, L., Gille, J.C., Barnett, J.J., Levelt, P.F., & Decola, P. (2006). Overview of the EOS aura mission. *IEEE Transactions on Geoscience and Remote Sensing*, 44, 1066-1074

Shen, Y., Jiang, F., Feng, S., Zheng, Y., Cai, Z., & Lyu, X. (2021). Impact of weather and emission changes on NO<sub>2</sub> concentrations in China during 2014–2019. *Environmental Pollution*, 269, 116163

Taylor, R. (1990). Interpretation of the Correlation Coefficient: A Basic Review. *Journal of Diagnostic Medical Sonography*, 6, 35-39

Wang, B., & Chen, Z. (2013). An intercomparison of satellite-derived ground-level NO<sub>2</sub> concentrations with GMSMB modeling results and in-situ measurements – A North American study. *Environmental Pollution*, 181, 172-181

Wu, X., Nethery, R.C., Sabath, M.B., Braun, D., & Dominici, F. (2020). Air pollution and COVID-19 mortality in the United States: Strengths and limitations of an ecological regression analysis. *Science Advances*, 6, eabd4049

Xiang, Y., Zhang, T., Liu, J., Lv, L., Dong, Y., & Chen, Z. (2019). Atmosphere boundary layer height and its effect on air pollutants in Beijing during winter heavy pollution. *Atmospheric Research*, 215, 305-316

Yao, Y., Pan, J., Liu, Z., Meng, X., Wang, W., Kan, H., & Wang, W. (2021). Ambient nitrogen dioxide pollution and spreadability of COVID-19 in Chinese cities. *Ecotoxicology and Environmental Safety*, 208, 111421

Yousefian, F., Faridi, S., Azimi, F., Aghaei, M., Shamsipour, M., Yaghmaeian, K., & Hassanvand, M.S. (2020). Temporal variations of ambient air pollutants and meteorological influences on their concentrations in Tehran during 2012–2017. *Scientific Reports*, 10, 292

Yu, D., Zhang, Y., Wu, X., Li, D., & Li, G. (2021). The varying effects of accessing high-speed rail system on China's county development: A geographically weighted panel regression analysis. *Land Use Policy*, 100, 104935

Zhao, Zhou, Li, Cao, He, Yu, Li, Elvidge, Cheng, & Zhou (2019). Applications of Satellite Remote Sensing of Nighttime Light Observations: Advances, Challenges, and Perspectives. *Remote Sensing*, 11, 1971

Zheng, Yang, Wu, & Marinello (2019). Spatial Variation of NO<sub>2</sub> and Its Impact Factors in China: An Application of Sentinel-5P Products. *Remote Sensing*, 11, 1939